Title of Dissertation

A Dissertation Presented

by

Yifan Fang

to

The Graduate School

in Partial Fulfillment of the

Requirements

for the Degree of

Doctor of Philosophy

in

Physics

(Concentration – optional)

Stony Brook University

May/August/ December 2024

(include this copyright page only if you are selecting copyright through ProQuest, which is optional)

Stony Brook University

The Graduate School

Yifan Fang

We, the dissertation committee for the above candidate for the

Doctor of Philosophy degree, hereby recommend

acceptance of this dissertation.

Name – Dissertation Advisor
Include title and department

Name - Chairperson of Defense
Include title and department

Type the remaining committee members using the above format. Type each member's name, title and department. Always make sure the signature page is kept to one page in length.

Type the outside member's name last. Include discipline and affiliation.

This dissertation is accepted by the Graduate School

Interim Dean of the Graduate School

Abstract of the Dissertation

Velocity-selective Resonances of the Adiabatic Rapid Passage Force in Metastable Helium

by

Yifan Fang

Doctor of Philosophy

in

Physics

(Concentration – optional)

Stony Brook University

2024

From optical tweezers to Doppler molasses and magneto-optical traps, optical forces have been a powerful tool for advancing control of quantum systems. Recent experiments have explored optical forces relying on stimulated emission rather than spontaneous emission. The Adiabatic Rapid Passage (ARP) force uses alternating chirped light pulses to excite and stimulate atoms providing a coherent momentum exchange. To determine the usefulness of the ARP force, we measure its velocity dependence. The velocity dependence contains large peaks in the magnitude of this force at regularly spaced velocity intervals, which suggests coherent effects in the ARP forces. This work demonstrates and discusses these velocity-selective resonances for various experimental parameters and lays out a roadmap for future work.

Dedication Page

To my parents Wei and Lu, to my husband Xiang

Table of Contents

List of Charts, Graphs, Illustrations

Acknowledgments

Use this page for your preface or introduction if applicable; please use only one of the titles for this page. Otherwise, you may delete it.

Chapter 1. Introduction

The use of optical forces to precisely control the motion of atoms has played a major role in expanding the field of atomic physics. However, in a majority of experiments, these optical forces are limited in strength by the inherent properties of the chosen atoms, mainly the rates of spontaneous emission, required to return the atoms to their ground state. It has been shown that the process of absorption, followed by stimulated emissions, can be used to provide a more rapid return to the atomic ground state. Through careful design of the experiment, a coherent exchange of momentum can take place, exerting a large force on the atoms.

One important application of the optical force is laser cooling and trapping, which was first introduced more than thirty years ago [1][2][3]. Originally, laser cooling was proposed to cool trapped ions which improves its precision measurement for high resolution spectroscopy [1][4]. Later, laser cooling was also applied to cool neutral atoms [2], which was first observed in 1981 [5].

As experimental techniques advanced, significant improvements in laser cooling, magnetic trapping, and evaporative cooling were made, enabling the observation of new and exciting phenomena. In 1995, these developments culminated in the groundbreaking achievement of Bose-Einstein Condensation (BEC) in a dilute atomic gas [6][7]. BEC occurs when a group of atoms is cooled to near absolute zero, causing them to occupy the same quantum state, behaving collectively as a single quantum entity. This achievement demonstrated the potential of ultra-cold atomic gases as a powerful tool for exploring quantum mechanics in a controlled laboratory setting.

An important property of the optical force is its velocity dependence. Forces that are effective for laser cooling must be strong at certain velocities and vanish at others, allowing for the compression of atoms initially spread across a broad velocity range into a region where the

force goes to zero. The effectiveness of such forces is determined by both their range and strength within the region where the force is finite. Radiative force can be used in laser cooling, such as the classical example of Doppler cooling [8]. However, for the radiative force, in the low-intensity limit, the range of the force is largely dictated by the atomic properties, such as transition frequencies. Therefore, it is desirable to investigate optical forces whose magnitude and range are independent of the specific properties of the atoms being cooled, ensuring broader applicability and potentially greater efficiency in cooling various types of particles.

Much greater forces that primarily rely on stimulated processes have been shown with poly-chromatic forces, such as bi-chromatic force [9] and Adiabatic Rapid Passage (ARP) forces [10]. These forces not only exert stronger forces over a shorter interaction length compared to radiative forces, but they also have a much larger velocity capture range. Further, due to their stimulated nature, they may also potentially be used in cooling molecules [11][12].

This thesis relates to one type of optical force that originates from coherent exchange of momentums based on simulated processes, Adiabatic Rapid Passage (ARP). In particular, the thesis presents interesting experimental findings related to the velocity dependence of ARP forces. As will be illustrated, in contrast to a naïve view of ARP's velocity dependence, in which the force is maxed at zero velocity and decreases gradually to zero, the ARP forces at some finite velocities are higher than others – showing a velocity selective resonance. Although previous experiments have also revealed similar peak and valley structures in the ARP force profile, the current thesis have demonstrated that these structures are real and consistent across different data runs, and have also provided, for the first time, a quantitative analysis on the peak and valley structures of the ARP force profile.

Chapter 1 first introduces the concept of two-level atoms as fundamentals in understanding optical forces and proceeds to an overview of three types of optical forces. Chapter 2 focuses the discussion on the theory of ARP, including how the force originates from an ARP process, various parameters that affect the magnitude of the ARP force and considerations related to multiple ARP pulses. Chapter 3 describes the experimental setup consisting mainly of a vacuum system and an optical system. Chapter 4 is dedicated to the experimental results showing the velocity dependence of ARP forces and discussions on the features of the ARP force profile. The last section of Chapter 4 lays out proposals for future ARP force detection methods that would potentially address the limitations of the current measurement scheme.

1.1 Two-Level Atom: Bloch Sphere and Optical Bloch Equation

A widely used model of studying atom-light interaction is by a two-level system [1]. To start, the time-dependent Schrödinger equation (TDSE) reads:

$$\mathcal{H}\Psi(\mathbf{r},t) = i\hbar\frac{\partial}{\partial t}\big(\Psi(r,t)\big) \tag{1.1}$$

$$\mathcal{H} = \mathcal{H}_0 + \mathcal{H}'(t) \tag{1.2}$$

$\mathcal{H}_0$ is the field-free atomic Hamiltonian and $\mathcal{H}'(t)$ is the interaction Hamiltonian describing the atom-light interaction. According to Ref. [16][17], the TDSE equation can be rewritten into:

$$i\hbar\frac{d}{dt}\Big(c_j(t)\Big) = \sum_k c_k(t)\mathcal{H}'_{jk}(t)e^{i\omega_{jk}t} \tag{1.3}$$

If an atom in a two-level system is driven by a light field with frequency ω_l and oscillates between a ground state |g> and an excited state |e>, then the TDSE can be further reduced to:

$$i\hbar\dot{c_g}(t) = c_e(t)\mathcal{H}'_{ge}(t)e^{-i\omega_a t} \tag{1.4}$$

$$i\hbar\dot{c_e}(t) = c_g(t)\mathcal{H}'_{eg}(t)e^{-i\omega_a t} \tag{1.5}$$

Here, ω_a is the resonant frequency of the atom, and the interaction Hamiltonian is $\mathcal{H}'_{ge} \equiv < g|\mathcal{H}'(t)|e >$, and c_e, c_g are complex amplitudes. There is both a time-independent part of the Hamiltonian, written as:

$$\mathcal{H}_0 = \frac{p^2}{2m} + V \tag{1.6}$$

And a time dependent part:

$$\mathcal{H}'(t) = -e\mathcal{E}(r,t) * r = -d * \mathcal{E}(r,t) \tag{1.7}$$

Here, $\mathcal{E} = \frac{1}{c}\frac{dA}{dt}$, and represents the coupling of the two levels by the electric field [13][14].

In an example of the light field being a z-direction propagating plane wave, $\mathcal{E}$ takes the form of:

$$\mathcal{E}(r,t) = E_0\hat{\epsilon}\cos(\omega_l t - k * z)\, e^{-i\phi} \tag{1.8}$$

The resulting time-dependent Hamiltonian $\mathcal{H}'(t)$ then becomes

$$\mathcal{H}'_{ge} = \hbar\Omega \cos(\omega_l t - k * z)\, e^{-i\phi} \tag{1.9}$$

where Ω is the Rabi frequency and it is defined to be

$$\Omega \equiv -\frac{eE_0}{\hbar} < e|r|g > \tag{1.10}$$

Accordingly, the coupled equations 1.4 and 1.5 of the TDSE can be rewritten as follows

$$\dot{c_g}(t) = -i\frac{\Omega e^{-i\phi}}{2}\left(e^{-i\omega_l t} + e^{i\omega_l t}\right)e^{-i\omega_a t}c_e(t) \tag{1.11a}$$

$$\dot{c_e}(t) = -i\frac{\Omega^* e^{i\phi}}{2}\left(e^{-i\omega_l t} + e^{i\omega_l t}\right)e^{i\omega_a t}c_g(t) \tag{1.11b}$$

Here, the Rotating Wave Approximation (RWA) [15] will be applied to further transform the TDSE. In RWA, the oscillating terms, such as $e^{-i\omega_l t}$, are treated differently depending on the timescale. For example, if the fast-oscillating terms, such as $e^{-i(\omega_l+\omega_a)t}$ is on the order of the optical frequency of Terahertz, then the average of this term in the duration of the experiment will likely be zero. On the other hand, the slow-oscillating terms, such as $e^{-i(\omega_l-\omega_a)t}$ is normally on the order of a few Megahertz and is more relevant to the time scale of the experiment. With the RWA approximation, 1.11a and 1.11b further reduce to:

$$\dot{c_g}(t) = -i\frac{\Omega e^{-i\phi}}{2}e^{-i\delta t}c_e(t) \tag{1.12a}$$

$$\dot{c_e}(t) = -i\frac{\Omega e^{-i\phi}}{2}e^{i\delta t}c_g(t) \tag{1.12b}$$

in which $\delta \equiv \omega_l - \omega_a$. Further decoupling the two equations with differentiation leads to:

$$\ddot{c}_g(t) - i\delta\dot{c}_g(t) + \frac{|\Omega|^2}{4}c_g(t) = 0 \tag{1.13a}$$

$$\ddot{c}_e(t) + i\delta\dot{c}_e(t) + \frac{|\Omega|^2}{4}c_e(t) = 0 \tag{1.13b}$$

The solutions to 1.13 a and 1.13 b yields the Rabi oscillation of $c_g(t)$ and $c_e(t)$ at a frequency defined by a generalized Rabi frequency $\Omega' \equiv \sqrt{|\Omega|^2 + \delta^2}$. A special situation is when the detuning δ is zero, and the Rabi frequency will drive a complete inversion of states, arrive at $|c_e(t)|^2 = 1$.

Another way to represent a state evolution of a two-level atomic system is by the Optical Bloch Equation. In particular, the TDSE can be rewritten by way of using a Bloch Vector. To this end, A density matrix ρ is introduced.

The density matrix ρ based on c_e, c_g provides an insightful way to explore the time-dependent interaction system described above, which is based on the work by Feyman, Vernon and Hellswarth [17]

$$\rho \equiv \begin{pmatrix}\rho_{gg} & \rho_{ge}\\ \rho_{eg} & \rho_{ee}\end{pmatrix} = |\psi><\psi| = \begin{pmatrix}|c_g|^2 & c_g c_e^*\\ c_e c_g^* & |c_e|^2\end{pmatrix} \tag{1.14}$$

They considered a change of variables to a rotating coordinate system [17] and arrived at an artificial state vector **R**, called the Bloch vector, where |**R**(t)|=1 and its three components {u,v,w} are given by:

$$u = \rho_{eg} + \rho_{ge} = 2Re\left[c_g(t)c_e^*(t)\right]\cos\phi(t) \tag{1.15a}$$

$$v = i\left(\rho_{ge} - \rho_{eg}\right) = 2Im\left[c_g(t)c_e^*(t)\right]sin\phi(t) \tag{1.15b}$$

$$w = \rho_{ee} - \rho_{gg} = |c_e(t)|^2 - \left|c_g(t)\right|^2 \tag{1.15c}$$

The Bloch vector can be pictured as moving on a unit sphere, called the Bloch sphere, where the south pole, with $w = -1$, represents the ground state of the system and the north pole, with $w = +1$, represents the excited state of the system. Accordingly, any other point on the Bloch sphere represents a superposition state of the system.

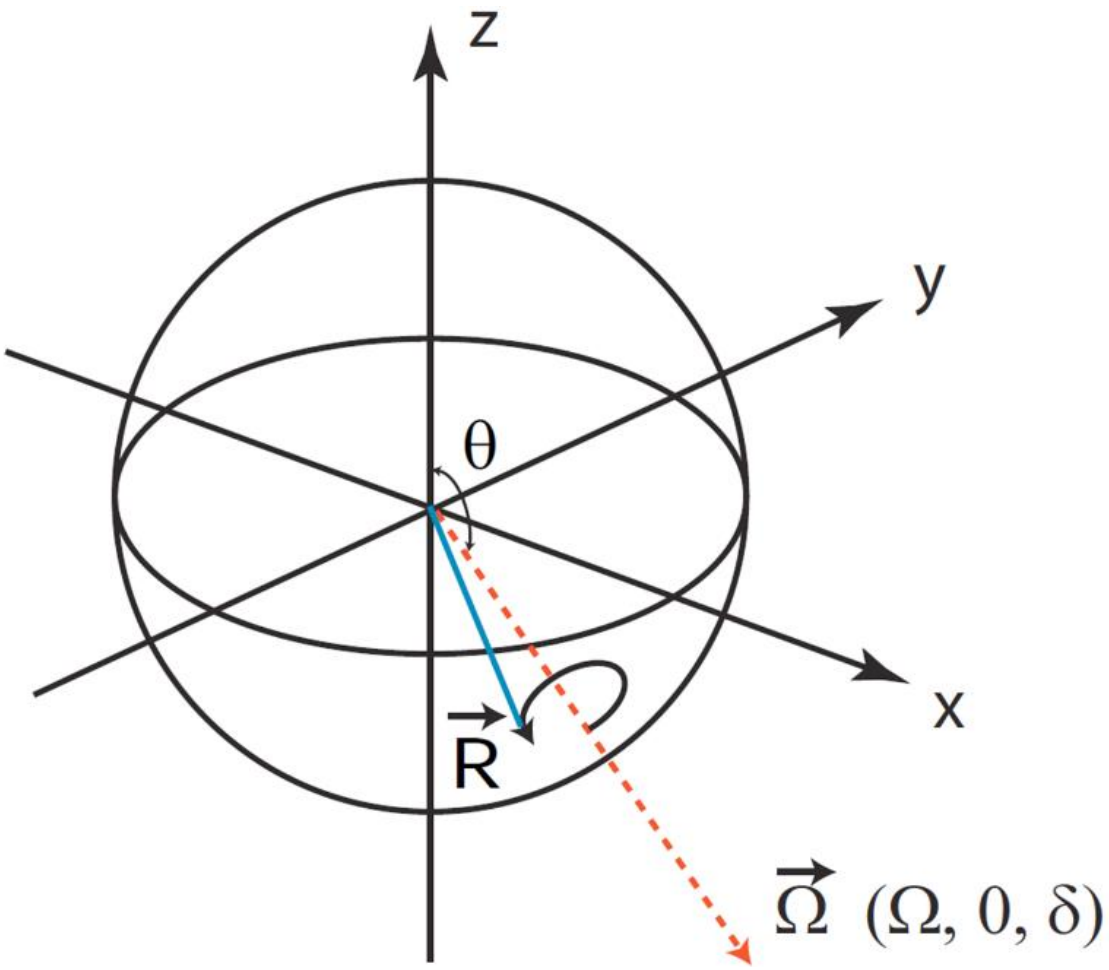

FIG.1. 1 A Bloch vector *R* processing around a torque vector Ω on a Bloch sphere. Picture adapted from Ref [18].

Using the Bloch vector representation, the TDSE of the two-level system can be rewritten as:

$$\frac{d\mathbf{R}}{dt} = \boldsymbol{\Omega} \times \boldsymbol{R} \tag{1.16}$$

Here, $\boldsymbol{\Omega}$ is called the torque vector and its components are $\{\Omega_{Real}, \Omega_{Imag}, -\delta\}$, where $\Omega_{Real}, \Omega_{Imag}$ are real and imaginary part of the Rabi frequency, respectively. $\delta = \omega_l - \omega_a$ and represents the detuning of the light frequency from the atomic resonance.

Spontaneous emission, or more generally, a decay term could be added to the Optical Bloch Equation of 1.16 to expand its application to realistic situations. Treating spontaneous emission with a decay rate γ as an inelastic collision [15],

$$\dot{u} = \Omega_{imag} w - \delta v - \left(\frac{\gamma}{2}\right) u \tag{1.17a}$$

$$\dot{v} = -\Omega_{real} w + \delta u - \left(\frac{\gamma}{2}\right) v \tag{1.17b}$$

$$\dot{w} = \Omega_{real} v - \Omega_{imag} u - \gamma(w + 1) \tag{1.17c}$$

1.2 Optical Forces

During an interaction between an atom of mass M and a light field with frequency ω_l, the linear momentum of the light, $\hbar\omega_l/c \equiv \hbar k$ transfers to the momentum of the atom, resulting in a velocity change of $v_r = \hbar k/M \sim$ a few cm/s. The magnitude of the force from this process depends on how many momentum exchanges happen during a certain time interval. Section 1.2.1 explores a radiative force resulting from a single frequency light field. Section 1.2.2 introduces a polychromatic force resulting from a multi-frequency light field.

1.2.1 The Radiative Force

First consider the simplest case of a stationary atom in a resonant laser field. As shown in this figure, a stationary atom in a resonant laser field will absorb light and move from ground to excited state. The momentum of the absorbed light, $\hbar k$ will also transfer to the atom resulting in a momentum change in the same direction the laser beam is traveling. After some time, the atom will undergo the process of spontaneous emission, which returns the atom to its ground state and emits light in a random direction. Since the light is carrying away $\hbar k$ of momentum, the atom will recoil in the opposite direction. Sometimes, this second momentum kick will be in a similar direction to the initial kick, other times it will be almost perfectly opposed, and yet other times, it could be almost orthogonal. Over many cycles, these secondary recoils will average out to zero, but the momentum changes for absorption are all additive, giving a net momentum change in the direction the light is traveling.

The total strength of the force depends on the repletion rate of this process. In this case, it is limited by the spontaneous emission rate, γ, which allows the atoms to return to its ground state. The force can simply be described by the momentum change per cycle multiplied by the repetition rate, or scattering rate γ. Quantitatively,

$$F_{rad} = \hbar k \gamma |c_e(t)|^2 \tag{1.11}$$

The force can be further written as, according to Ref. [1]

$$F_{rad} = \frac{\frac{\hbar k s_0 \gamma}{2}}{1 + s_0 + \left(\frac{2\delta}{\gamma}\right)^2} \tag{1.12}$$

Where s_0 is the saturation parameter given by

$$s_0 = 2\left(\frac{|\Omega|}{\gamma}\right)^2 = \frac{I}{I_{sat}} \tag{1.13}$$

Where I_{sat} is the saturation intensity and $I_{sat} \equiv \pi hc/3\lambda^3\,\tau$. When the light intensity is much higher than the saturation intensity, and the light frequency matches the atomic resonance frequency, such that $\delta = 0$, we get the maximum of F_{rad} to be

$$F_{rad,max} = \frac{\hbar k\gamma}{2} \tag{1.14}$$

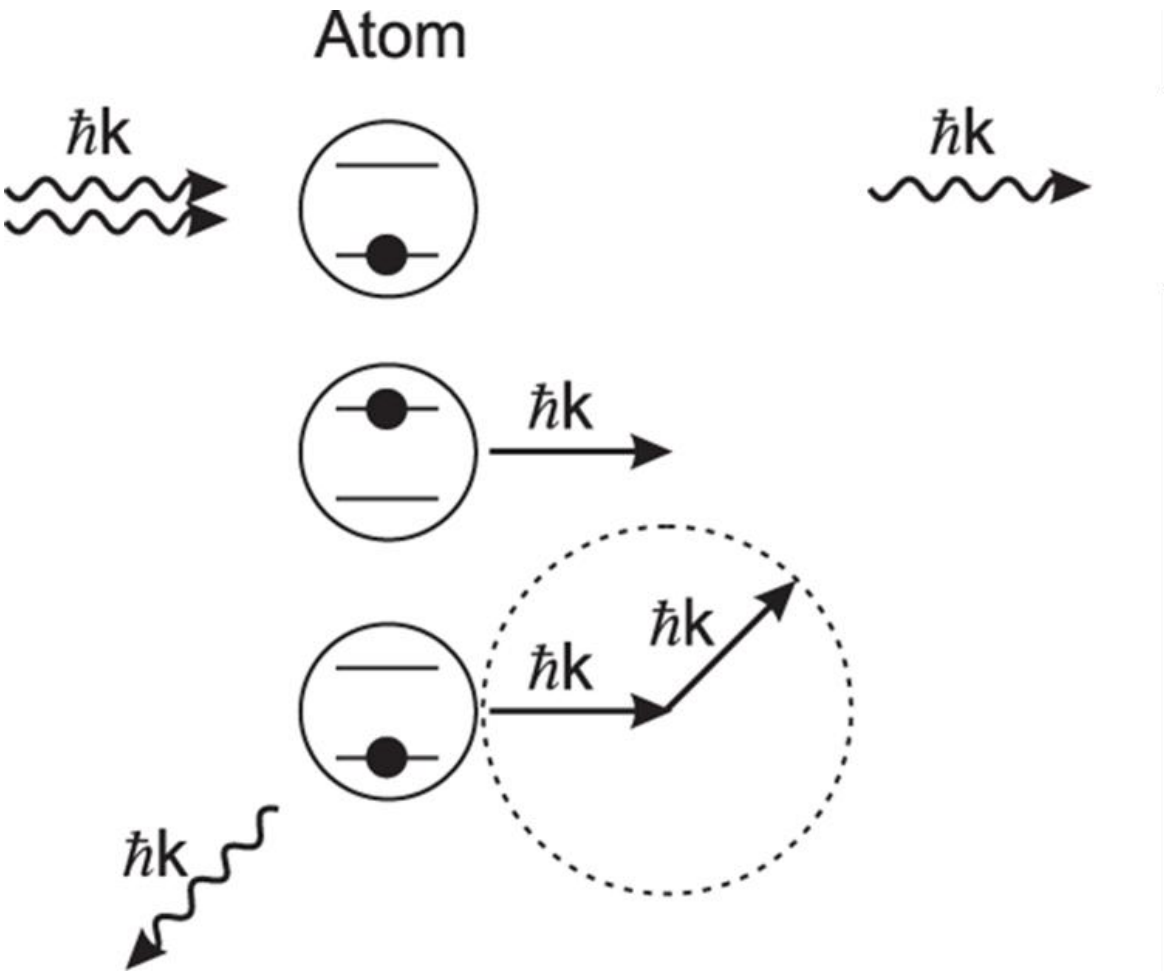

FIG.1.2: Radiative force production cycle. Picture adapted from Ref [18]

1.2.2 The Polychromatic Force

In the field of laser cooling, the use of a polychromatic force offers significant advantages over traditional radiative forces that rely on spontaneous emission. Unlike radiative forces, which are inherently tied to the emission of photons and can lead to unwanted heating or decoherence, the optical force generated by polychromatic light does not rely on spontaneous emission. This is crucial for achieving more efficient and controlled cooling. The key mechanism behind such forces often involves interactions between atoms and light fields of varying frequencies, leading to novel ways to manipulate atomic motion without the deleterious effects of photon re-emission.

One important example of a polychromatic force is the dipole force, which arises from the interaction between atoms and a light field that creates a gradient in the light intensity. The dipole force is typically employed in optical traps, where atoms are attracted to regions of high light intensity, enabling precise control over atomic positions. Another relevant force is the bi-chromatic force, which involves two laser fields of slightly different frequencies. The interaction between these two fields leads to a force on atoms that can result in cooling or trapping without the need for spontaneous photon emission. Lastly, the Adiabatic Rapid Passage (ARP) force is a phenomenon in which an atom is subjected to a frequency sweep of light. If the sweep occurs

sufficiently slowly, the atom remains in an adiabatic state and experiences a force that can also lead to cooling, exploiting the resonance between the atom's energy levels and the time-varying light field. Each of these forces highlights how polychromatic light, through carefully engineered interactions, can provide a powerful means to control atomic motion without the limitations imposed by radiative losses.

The ARP force will be the major focus of this thesis. The next few chapters will lay out the theory of ARP, the experimental setup and discuss the properties of the ARP force based on the results.

Chapter 2: Adiabatic Rapid Passage (ARP)

This chapter relates to the theory of an ARP force. The chapter starts with a discussion (section 2.1) on two physics pictures to describe an ARP process and calculations of the resulting ARP force. Then the chapter proceeds to discuss (section 2.2) how different parameters of an ARP pulse affect the magnitude of the ARP force. Following the discussion of a single ARP pulse, the chapter then discusses (section 2.3) ARP force resulting from multiple ARP pulses and various factors that affect properties of the ARP force in the multiple pulses scenario.

2.1 Theory of ARP

Adiabatic Rapid Passage (ARP) is well-known in the magnetic resonance community [20]to invert the population of a two-level system. In the optical regime, an ARP process requires that the frequency of a light pulse is swept through the resonant frequency of a two-level atom in a time much shorter than the time scale of spontaneous emissions $\tau = 1/\gamma$. A series of properly tailored, counterpropagating and frequency-swept light pulses imparting on the atom lead to a momentum exchange of $2\hbar k$ between light fields and the atom in each cycle[21]. As a result, the force $F_{ARP} = 2\hbar k/T$ with T being the repetition rate of theses cycles can be much larger than a radiative force, $F_{rad} = \hbar k\gamma/2$ given $\frac{1}{T} \gg \gamma$.

2.1.1 Dressed Atom Picture and Bloch Sphere Picture

An ARP process of a two-level atom can be visualized in both a dressed atom picture and a Bloch sphere picture. This section discusses the adiabaticity and rapidity of the ARP process both in view of a dressed atom picture and in view of a Bloch sphere picture.

Following detailed explanations on dressed atom picture laid out in [22] [23] the dressed atom Hamiltonian for a two-level system can be written as

$$H(t) = \frac{\hbar}{2}\begin{pmatrix} \delta(t) & \Omega(t) \\ \Omega(t) & -\delta(t) \end{pmatrix} \tag{2.1}$$

We can diagonalize this to find the eigen-energies to be

$$E(t)_{\pm} = \pm(\hbar/2)\sqrt{(\delta(t))^2 + (\Omega(t))^2} \tag{2.2}$$

To better understand the eigenstates, we can plot the eigen-energies for both Rabi frequency and detuning as in FIG. 2.1, showing two eigen-energy sheets for a dressed two- level atom. There are some important aspects of the two eigen-energy sheets that are worth noting. First, when $\Omega(t)$=0, the dressed states resolve to the bare atomic states. Second, the ground and excited states |g> and |e> are otherwise mixed on two eigen-energy sheets away from the low intensity limit (characterized by $\Omega < \delta$) [24]. Third, the upper sheet changes from |g> to |e> as the detuning δ changes sign.

An ARP process in this dressed atom view involves a synchronized sweep of both the amplitude and frequency of the light such that the atomic state follows a path similar to a sample trajectory shown below in FIG. 2.1 on a chosen eigen-energy sheet during the transition between |g> and |e>. For this sample trajectory, $\delta(t) = \delta_0 \cos(\omega_m t)$, $\Omega(t) = \Omega_0 \sin(\omega_m t)$, and the time to make this transition is $T = \pi/\omega_m$, with ω_m being the modulation frequency charactering the sweeping rate of the trajectory, which is a tunable experimental parameter.

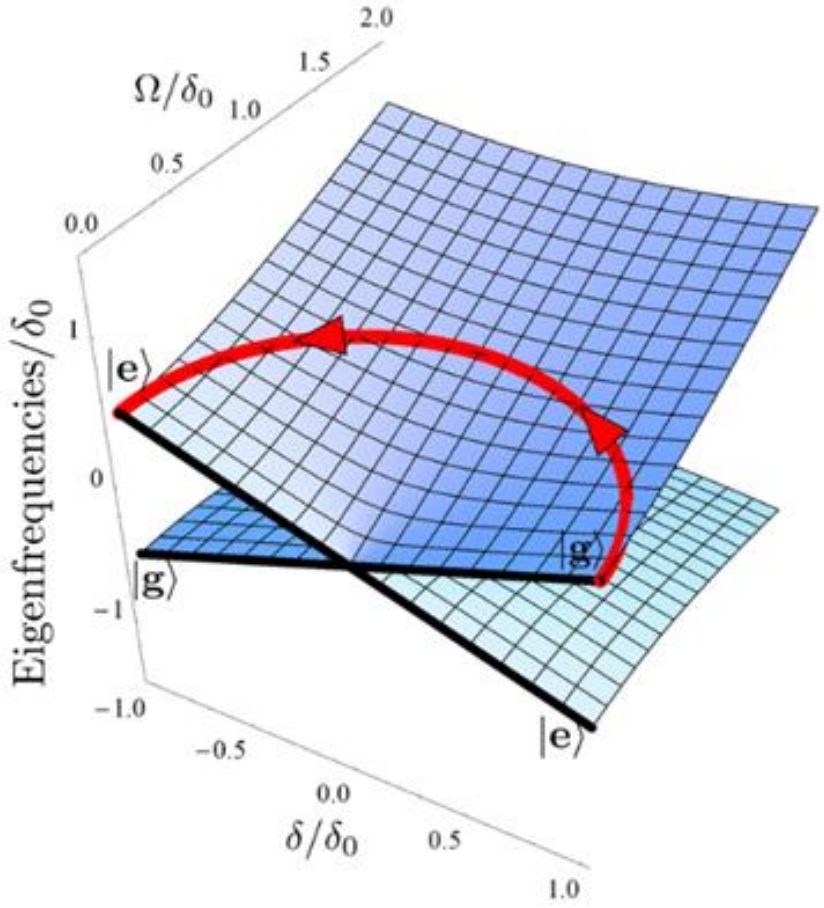

FIG.2.1: Energy of the dressed states comprise two separated sheets except at the conical intersection at the origin. The upper (lower) state is ground at $\boldsymbol{\Omega = 0}$ for $\boldsymbol{\delta > 0}$ ($\boldsymbol{\delta < 0}$). The indicated path is a possible trajectory of ARP. Picture taken from Ref [18].

In order to meet the "adiabatic" condition of the ARP process, the atomic state has to be swept slowly enough (small ω_m) to remain within a chosen eigenstate during the transition between |g> and |e>. However, since there is always a possibility of spontaneous decay occurring at rate γ during the transition, the "rapid" condition requires that the sweeping rate $\omega_m \gg \gamma$.

In fact, the conventional ARP parameter relation is:

$$\delta_0 \sim \Omega_0 \gg \omega_m \gg \gamma$$

And the reason is most easily understood from another picture, called Bloch sphere picture that is discussed below.

The Bloch vector description of the eigenfunctions allows a particularly graphical interpretation of ARP. The process consists of sweeping the optical frequency from one side of resonance to the other, so that the torque vector $\Omega(t)$ starts and ends nearly along the polar axis, but sweeps through the equatorial plane at $\delta(t)$=0. At the beginning of the frequency sweep, where the magnitude of the initial detuning δ_0 is much larger than Ω, the Bloch Vector R executes small, rapid orbits near the south pole (atom in the ground state). Then, as $\delta(t)$ approaches zero and $\Omega(t)$ reaches its maximum value of Ω_0, the axis of these orbits slowly drifts up toward the equator. The sweep continues toward the opposite detuning so that near the end of the sweep, where again $\delta(t)$ >> $\Omega(t)$, the Bloch Vector R executes small, rapid orbits near the north pole and is finally left at the north pole (the atom is in the excited state).

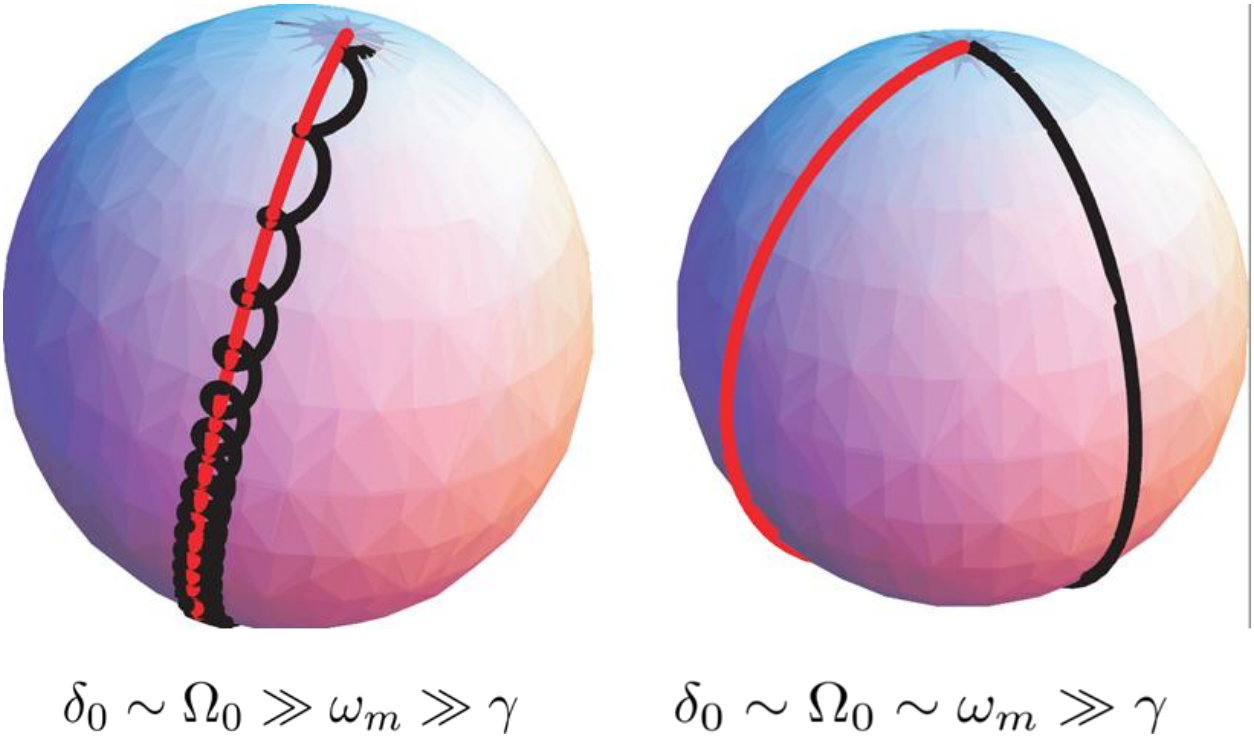

FIG.2.2: Bloch Sphere adopted from Ref [25]

The traditional constraints for this process to occur efficiently can be understood from two aspects. First, the Torque Vector $\Omega(t)$ must be large enough so that the Bloch Vector R makes very many precessions about $\Omega(t)$ during the seep time here given by $T = \pi/\omega_m$, where ω_m is the sweep rate, leading to $\Omega(t) >> \omega_m$ and explains "Adiabatic" in ARP. Second, the sweep rate ω_m needs to be much larger than the spontaneous rate γ, as discussed in the dressed atom picture and explains "Rapid" in ARP. These are the two conditions on the Rabi Frequency $\Omega(t)$ and sweep rate ω_m that must be met independently.

However, it has been shown in [23] that $\Omega(t)$ orbits like that shown on the right can also produce robust population inversion. The parameters are well outside the usual ARP domain and

will be hereby referred to as the unconventional region of parameter space, as opposed to the conventional region of parameter space commonly used by the magnetic resonance community. By relaxing the adiabatic condition of ARP, the pulse duration $T = \pi/\omega_m$ may be decreased, which leads to faster absorption stimulated emission cycles, and therefore larger optical forces at reasonable values of Ω_0, which means less light is required.

2.1.2 Calculation of ARP

Here is a finger physics description of ARP and the quantitative descriptions of ARP will follow in the next paragraph. FIG. 2.3 is a schematic for the ARP force. An atom begins in the ground state. An ARP pulse from the left causes absorption, exciting the atom and imparting $\hbar k$ momentum. An ARP pulse from the right causes stimulated emission; returning the atom to the ground state and imparting another $\hbar k$ momentum change in the same direction as the first.

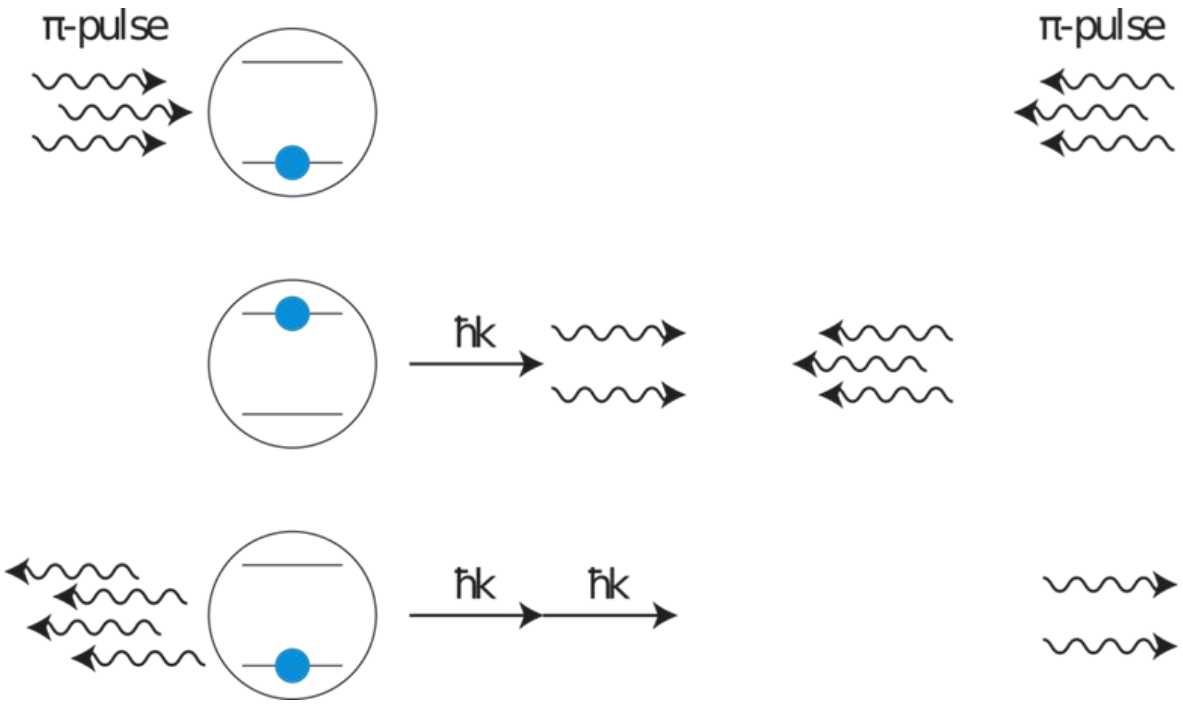

FIG.2.3: Schematic of the ARP force. A left ARP pulse excites the atom initially in the ground state and imparts a $\hbar\boldsymbol{k}$ momentum, then a right ARP pulse returns the atom to the ground state by stimulated emission so that overall there are 2 $\hbar\boldsymbol{k}$ being transferred to the atom by the light field. Picture taken from Ref [18]

The calculation of the ARP force on an atom starts with the Ehrenfest theorem Ref [26].

$$\vec{F} = Tr[\rho \nabla H] \tag{2.3}$$

For the case of one-dimensional, counter-propagating optical fields whose wavenumber is k, the force can be rewritten as

$$F = \frac{\hbar k}{2}\left(\left(\vec{\Omega}_{right} - \vec{\Omega}_{left}\right) \times \vec{R}\right)_3 \tag{2.4}$$

here Ω_{right} and Ω_{left} are the torque vectors of the right and left propagating fields. These experiments consider the case of non-temporally overlapped pulses. Therefore, at any point in time only right/left is considered. Thus, the force simplifies to

$$F = \pm\frac{\hbar k}{2}\left(\left(\vec{\Omega}_{right\ or\ left}\right) \times \vec{R}\right)_3 = \pm\frac{\hbar k}{2}\dot{w} \tag{2.5}$$

for a single pulse of duration π/ω_m

$$F = \frac{\hbar k}{2}\frac{\omega_m}{\pi}\Delta w \tag{2.6}$$

leading to a maximum $F_{ARP} = \hbar k\omega_m/\pi$ for an ideal transition from north pole to the south pole on the Bloch sphere. This is an expected result showing that the force on the atom is directly related to the change in w after interacting with the light and it lines up with our finger physics result.

2.2 ARP Force Parameters

As shown in FIG. 2.2, both conventional and unconventional ARP parameters can achieve a population inversion for a two-level atom resulting in a large force. This phenomenon may also be understood by simulating the ARP force on an atom [27]. FIG. 2.4 plots the ARP force as function of Ω_0 and δ_0 for a single pulse pair. The color scheme shows the force in units of F/F_{ARP}. For large values of Ω_0 and δ_0, the force is uniform and large (see white upper-right region). As Ω_0 and δ_0 get smaller and approach the unconventional parameter region, the force becomes more sensitive to the values of Ω_0 and δ_0. Nonetheless, it can be seen that even in the lower left corner, there are still regions with strong forces (within the lower-left red square.)

Since it's easier to access the unconventional parameter space (e.g., due to smaller Ω_0 resulting from limited optical power of laser) in the experiment, investigation of the ARP force in this thesis is carried out based on parameter sets in the unconventional parameter space.

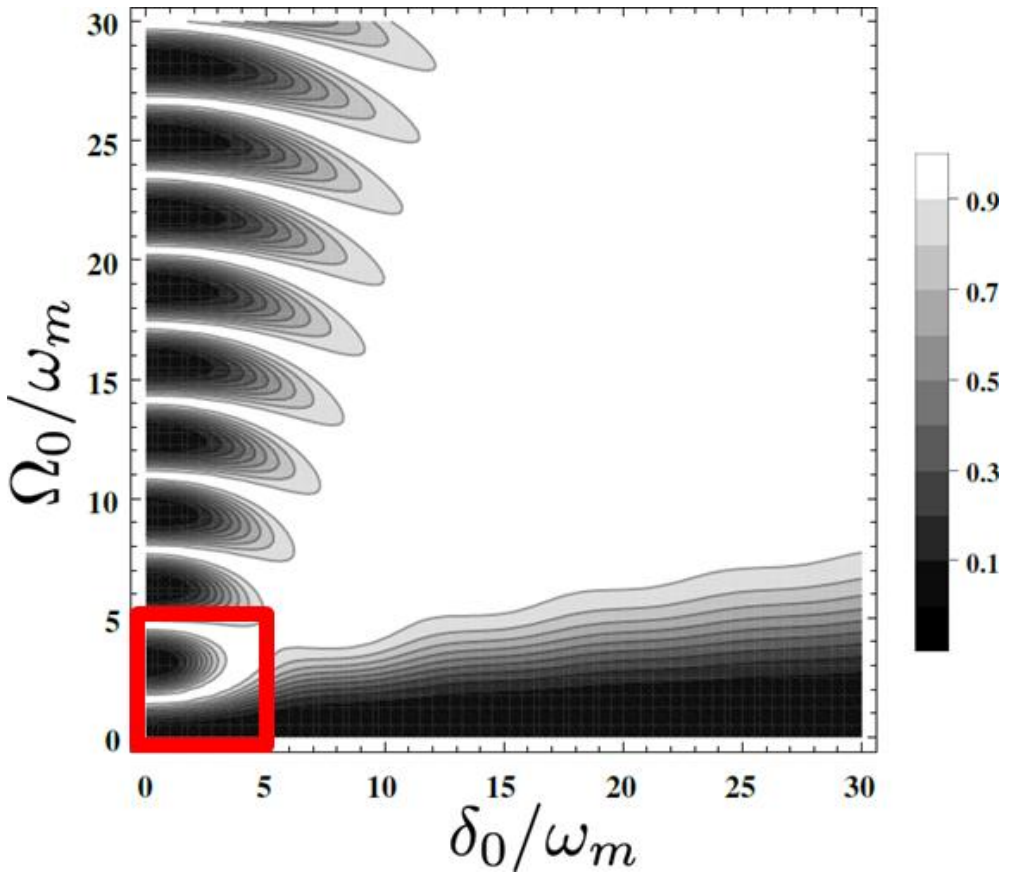

FIG.2.4: Plot of the ARP force as a function of $\boldsymbol{\Omega_0}$ and $\boldsymbol{\delta_0}$ for a single pulse pair, adopted from Ref [25].

2.3 Multiple ARP Sequences

Ideally, many absorption-stimulated emission cycles will impart a large momentum change to an atom, resulting in a large force. However, there are a number of situations that lead to a reduced force magnitude, which are described in the following sections. Specifically, section 2.3.1 discusses regions of imperfect pulses in a force map, such as FIG. 2.4, when the pulse number is large. Section 2.3.2 discusses the effects of spontaneous emission that happens during a pulse duration.

2.3.1 Imperfect pulse

Here, imperfect pulses refer to pulses that fail to fully invert the two-level atom system. FIG. 2.5 shows a comparison of optimal force regions for a single pulse pair (Left) and 320 pulse pairs (Right). According to the color scale, in which 'red' regions correspond to the largest ARP force, it is clear that the optimal force regions are much narrower in the case of 320 pulse pairs compared with that of a single pulse pair. This means that, as the number of pulse pairs "seen" by the atoms increases, the ARP force is increasingly sensitive to Ω_0 and δ_0. One cause of the sensitivity is the phase differences between pulses, ϕ_{rel} and ϕ_{pp}, caused by atomic action and the jitter of the timing that starts each sequence, respectively. ϕ_{rel} is the relative phase between the left and right pulses, ϕ_{pp} is the pulse-to-pulse phase difference between adjacent left or right pulses. In the experiment, the atomic beam spans a spatial extent much larger than a single wavelength, such that the average phase ϕ_{rel} can be estimated to be an average value over all possible relative phases, that is from 0 to π. Detailed discussion on the effect of phase can be found in Section 2.2.1 of [27]. In the simulation of the force map presented here, theses experimental effects are taken into account by averaging ϕ_{rel} over 0 to π.

The ARP force's sensitivity to Ω_0 and δ_0 can be further seen on the lower left corner of the force map, which corresponds to the accessible region in the experiment. FIG. 2.6 are zoomed in force maps of FIG. 2.5, focusing on the lower left corner. Looking at FIG. 2.6 (c), there are two regions that indicate strong ARP forces – the first region in the leftmost region of the force map and spans a crescent shape, and the second region in the upper right region of the force map and is titled sharply clockwise from the first crescent. It should be noted that the ARP force parameters Ω_0 and δ_0 chosen in the experiment (see Chapter 4, Results) come from the second region. Detailed discussion about force parameters can be found in Chapter 6 of Ref [18].

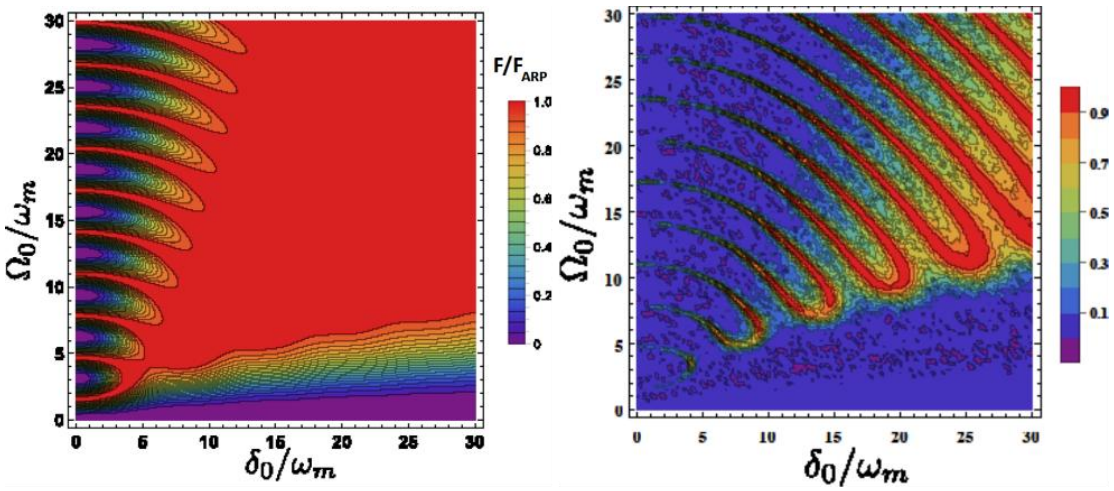

FIG.2.5: Left: ARP force magnitude, represented by a color scale, as a function of $\boldsymbol{\Omega_0}$ and $\boldsymbol{\delta_0}$ for a single pulse pair. Right: ARP force magnitude for 320 pulse pairs. Reproduced from Ref [18].

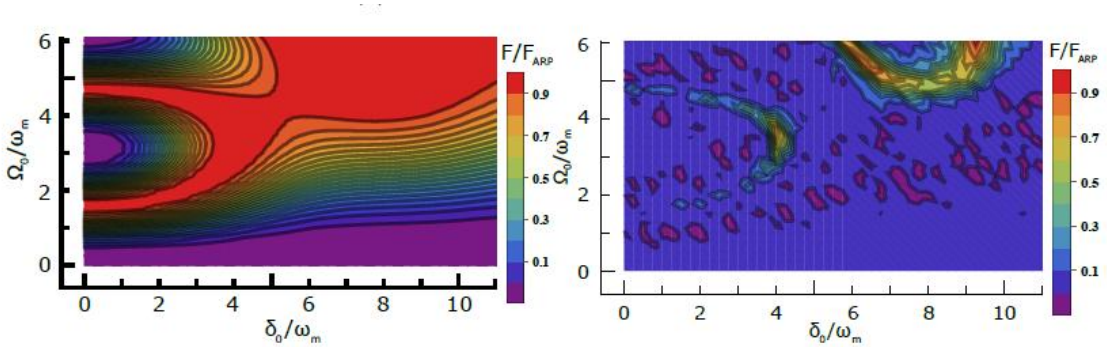

(b) Simulation, 1 pulse pair. (c) Simulation, 320 pulse pairs.

FIG.2.6: Zoomed in force maps of the lower left regions of FIG. 2.5. Reproduced from Ref [18].

2.3.2 Dead Time between adjacent ARP Pulse Pairs

Even though an individual ARP process can be much faster than the spontaneous decay rate, for a large enough number of pulses, spontaneous decay will need to be accounted for. A single spontaneous decay would reverse the ARP cycle: pulses intended to be absorbed would now cause stimulated emission and vice versa. This would also reverse the net momentum change per two pulse cycle and thus reverse the force.

One possibility for addressing this concern is to introduce "dead time", i.e., a period of time without light between the pairs of pulses, see FIG. 2.7. The reason that we chose $2\pi/\omega_m$ as the dead time is best explained in this simulated result of force vs number of pulse pairs for various values of the dead time between pulse pairs, in FIG. 2.8. The solid curve is for zero dead time, and the increasingly smaller dashes correspond to π/ω_m to $4\pi/\omega_m$ times respectively. For zero dead time, the ARP force is reduced to zero after a small number of pulse pairs because of increased probability of force reversal during a pulse sequence. However, the inclusion of dead time allows for the ARP force to be maintained over many more pulse pairs. The $2\pi/\omega_m$ value for dead time maintains the greatest force over very many pulse pairs and is used in our experiment.

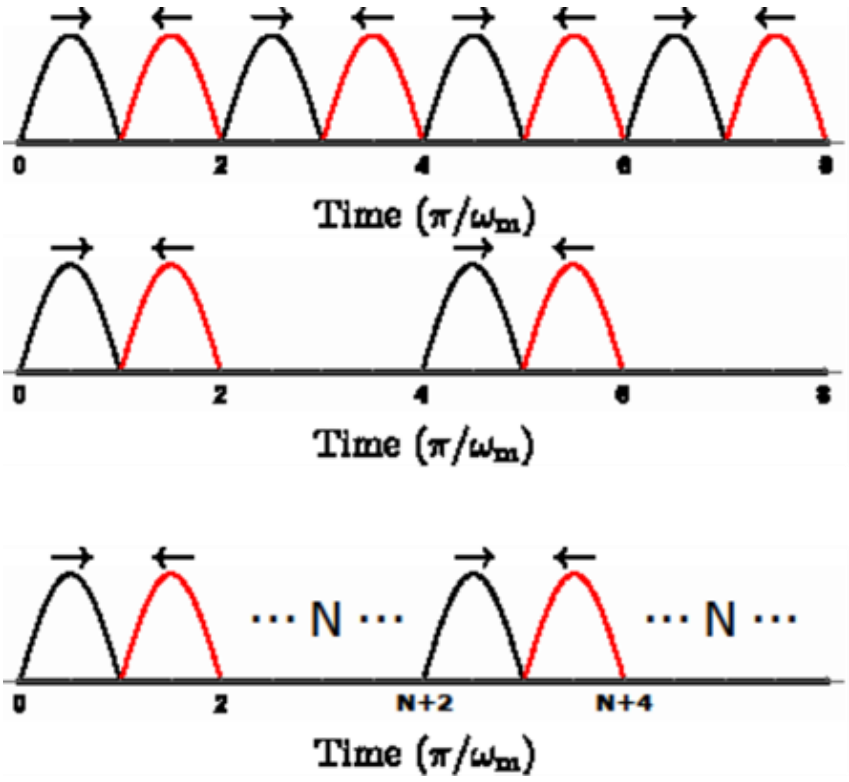

FIG.2.7: A schematic diagram of the timing scheme of the multiple ARP sequence. Reproduced from Ref [25]

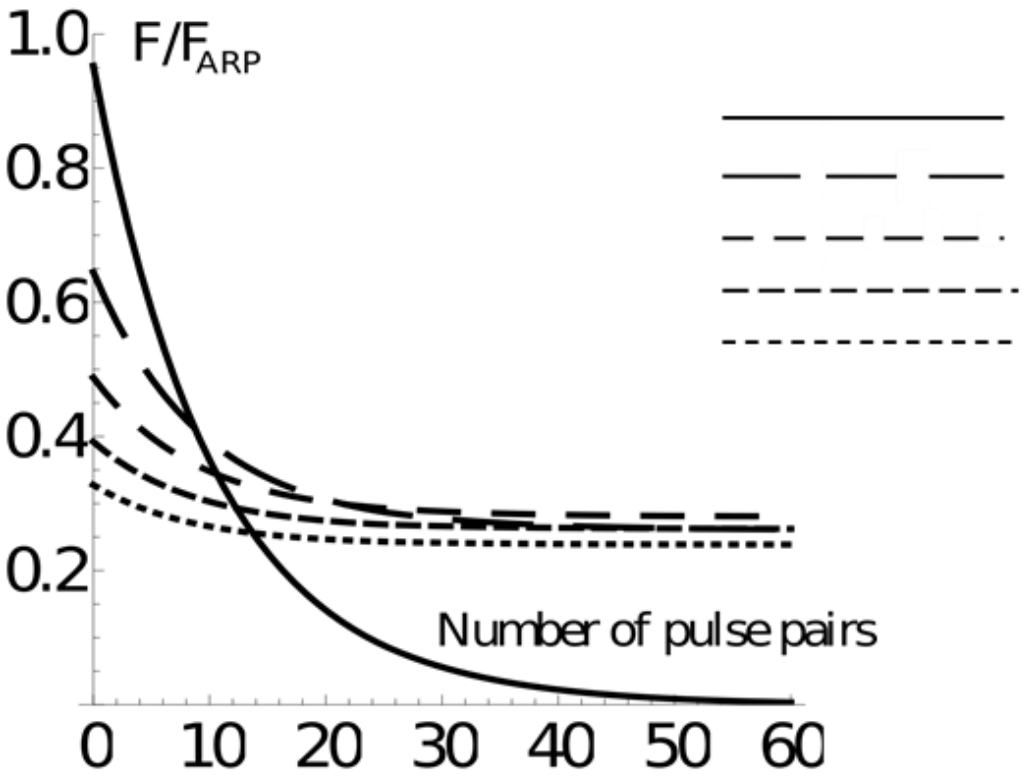

FIG.2.8: The calculated force vs. pulse pair numbers for various length of dead time. Reproduced from Ref. [25].

Chapter 3: Experiment

This chapter relates to the experimental setup, including Helium atom apparatus, vacuum system and optical system. The chapter will start with a discussion on properties of metastable He atoms (He*) and apparatus to produce He* atoms. Then the chapter proceeds to an introduction to the vacuum system in which He* atoms travel and interact with the ARP light. Lastly the chapter discusses the optical system and electronic modulators designed for producing the ARP light.

3.1 Helium Atom Apparatus

This experiment uses metastable Helium as the atomic species and works on the 2^3S_1 to 2^3P_2 transition shown in FIG. 3.1. This is an ideal transition for ARP to work on due to the rather long lifetime of the excited state. The large separation between the adjacent J levels means the transition can be well-approximated as a two-level system.

3.2 Vacuum System

This section introduces the vacuum system in the ARP experiment. A more detailed description of each component can be found in previous theses [23]. and won't be repeated here. Instead, the current discussion focuses on several differences compared with previous settings. It starts with an overview of the vacuum system and then moves to discussions about individual parts.

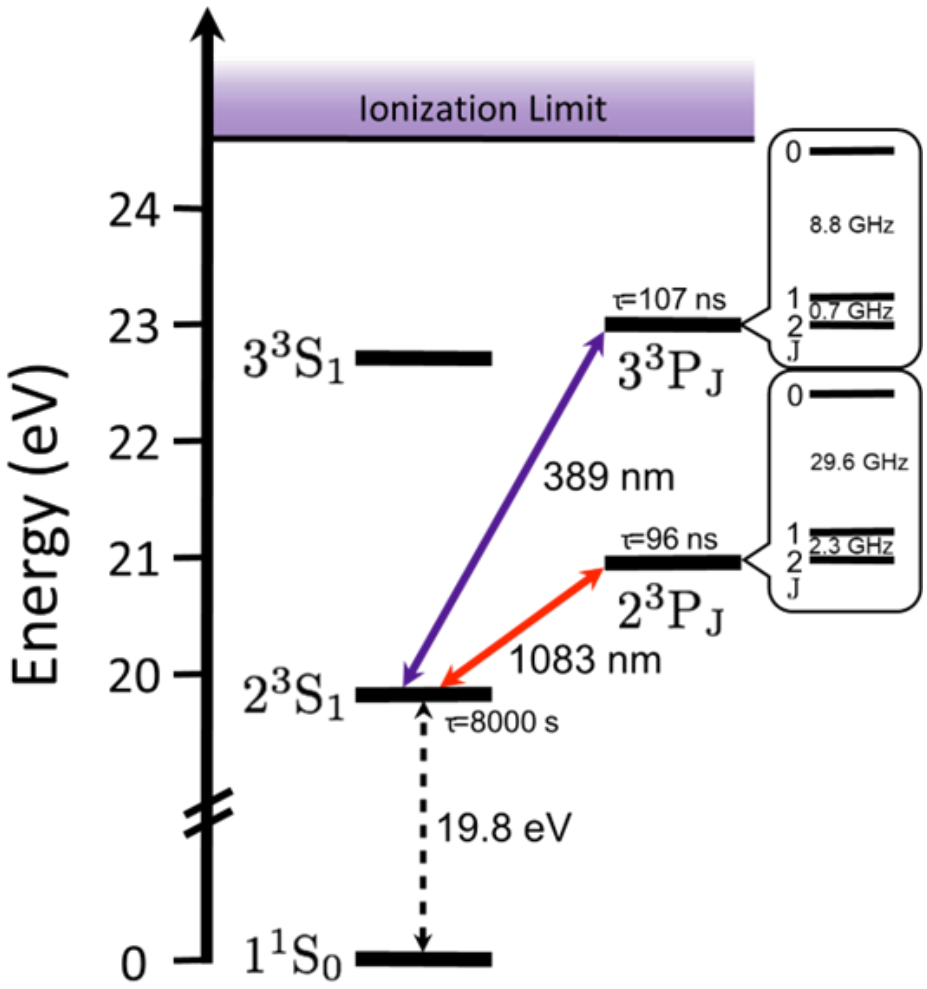

FIG.3.1: Relevant energy levels for the ARP experiments in helium. The lifetime of the metastable state 2^3S_1 is about 7900s and serves as the ground state for our experiments. Ref [28].

The vacuum system can be divided into mainly three sections: the metastable helium source, the interaction chamber, and the detection chamber. FIG. 3.2 is a schematic diagram of the vacuum system. The source region is pumped by a Pfeiffer TPH 300 turbo pump and a backing mechanical pump Pfeiffer Duo 110, so that when the source is off, the pressure in the source region is ~ 10^{-6} Torr, with the backing pressure ~10^{-3} Torr. When the source is on, most of the helium influx from 'He in' is pumped out through the 'He out' port with another mechanical pump, while the rest of the helium flows into the vacuum and He* atoms are produced near the end of the source region. He* then enters the interaction chamber, which is separated by a 0.5 mm aperture on a skimmer plate from the source region to enable differential pumping. The interaction chamber is pumped also by a Pfeiffer TPH 330 turbo pump and a backing pump of Welch 1376. He* atoms meet with counterpropagating ARP pulses in the interaction chamber and are then deflected from their original path by the ARP force, where their final positions are recorded by the MCP+PS detector placed downstream in the detection chamber.

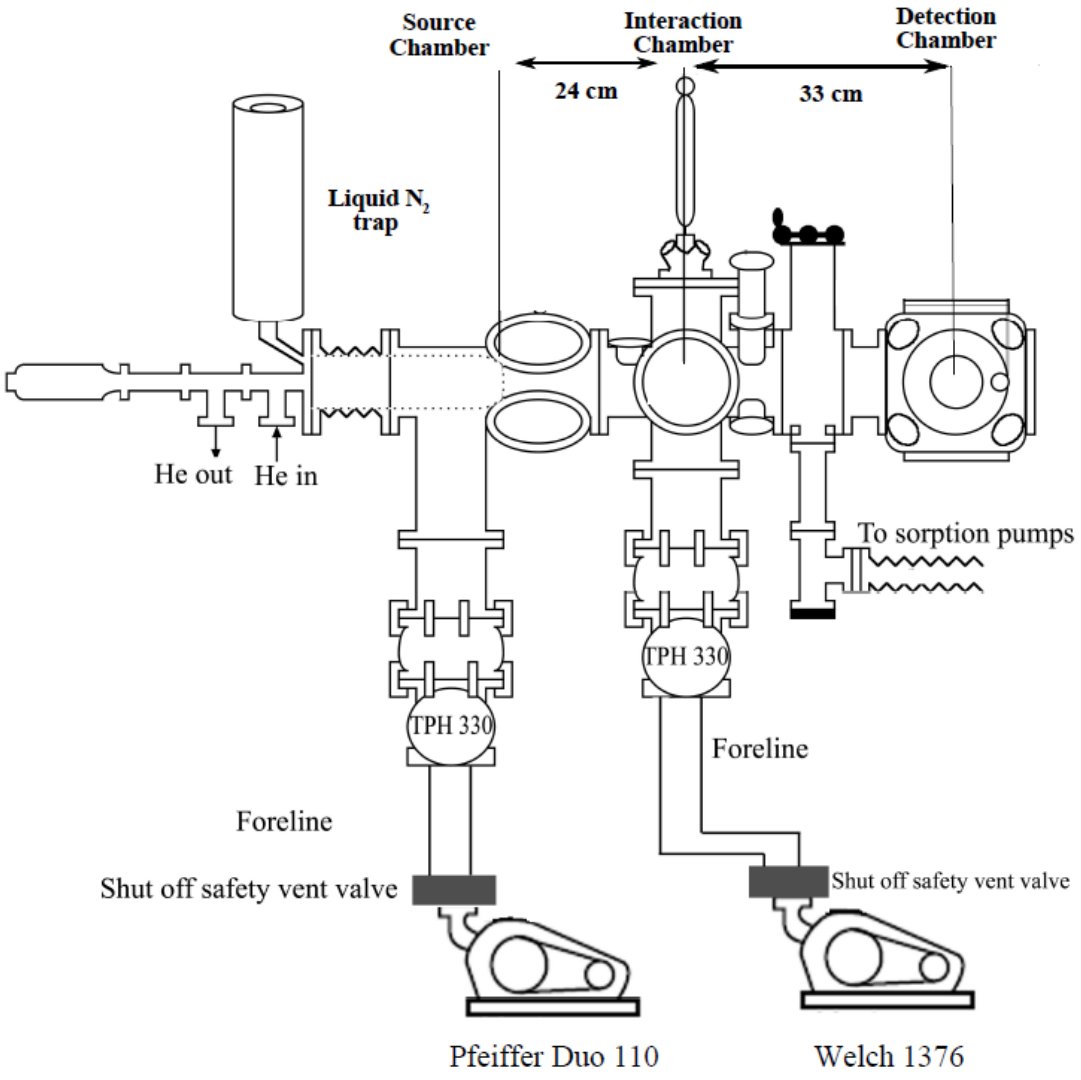

FIG.3.2: Schematic diagram of the vacuum system consisting of three sections. The distance between the nozzle plate where He* atoms are created and the point where ARP interacts with He* spans about 24 cm, and the distance from the interaction to the detector is about 33 cm.

Source Region:

The metastable helium source generates atoms in the 2^3S state via reverse flow and DC discharge [29] and the schematic is shown in FIG. 3.3. Helium flows into the source region through 'He In' port, travels between the glass tube and the steel jacket and meets with the high voltage tungsten needle towards the tip of the tapered glass tube, where a discharge is formed between the tip of the needle (cathode) and the nozzle plate (anode). Both singlet and triplet states of He* are produced in this discharge formed plasma via electron-ion recombination, and some triplet state atoms will survive to go through the skimmer plate although most of He* are quenched due to collisions. One thing to note is how various factors affect the reliable production of a Helium discharge and the subsequent He* beam. The first and foremost things to make sure of are the cleanliness of the glass tube, the sharpness of the tungsten needle and the quality of the anode surface. From past experience, a dim discharge glow, hence insufficient amount of He* production could result from dirty glass tube or "forks" developed at the tip of the needle. It is recommended that the source (sharpening of the needle and cleaning of the parts) should be maintained every two years [23]. Moreover, different pressure in the discharge region and voltage on the discharge needle can vastly change the quality of the Helium discharge, and therefore need to be carefully tuned to ensure a high quality He* production. The pressure in the discharge region can be regulated by adjusting the fine needle valve in the inlet region, and the typical reading of the inlet pressure is between 5 to 13 Torr when the source is lit. The discharge voltage is normally set to be between 2100 V to 2500 V, and we aim to obtain a discharge current over 2 mA in order to get the discharge run stably [23]. The values that optimized the He* discharge production in the current experiment are recorded here for future reference. Discharge voltage: 2100 V, discharge current: 2 mA, inlet pressure: 5 Torr.

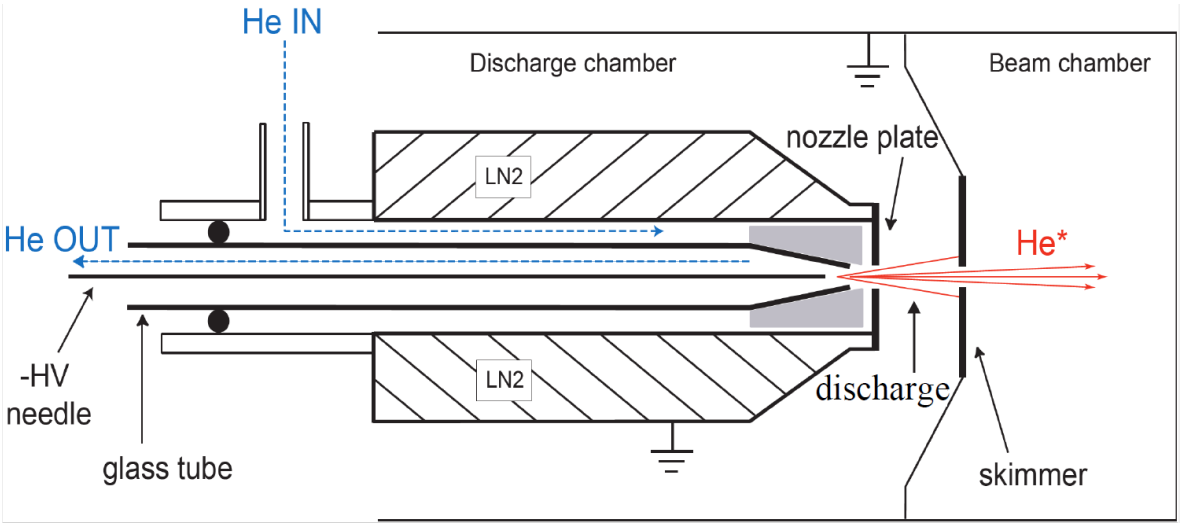

FIG.3.3: Top-view schematic of the reverse flow DC discharge source for He* production from Ref [27].

Interaction Chamber:

After passing through the aperture in the skimmer plate with a longitudinal velocity of roughly 1000 m/s [23], He* atoms enter the interaction chamber. A slit of 250 μm width and 1 cm height is located 24 cm away from the skimmer plate (See FIG 3.4 (a)) and is used to define the transverse velocity of the He* beam to be within $\pm 1 m/s$. There is a pair of Helmholtz coils mounted behind the slit (See FIG. 3.4 (b)) and it provides a homogeneous magnetic field which is perpendicular to the trajectory of the He* beam. The magnetic field serves to optically pump the He* atoms before interacting with the circularly polarized ARP pulses. However, there is no clear difference between our measured force profiles with or without the magnetic field.

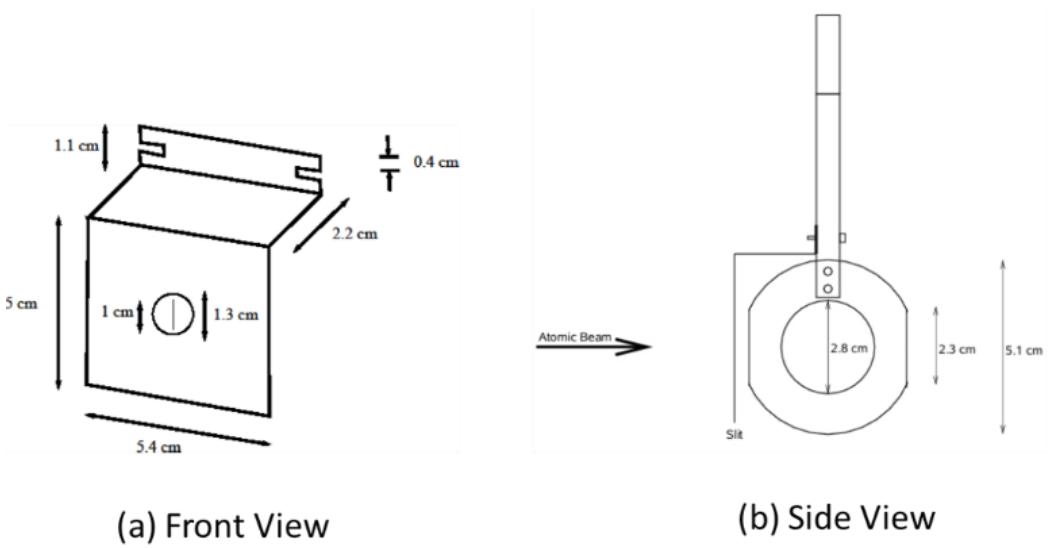

FIG.3.4: (a) and (b) are front and sides views of the slit which defines the atomic beam. The Helmholtz coils and the mount can be seen in (b) [27].

Detection Chamber:

The final position of deflected He* atoms are recorded by a MCP+PS detector assembly shown in FIG. 3.5. The MCP (Multi Channel Plate) is normally biased at negative 1000V, which provides multiplication and acceleration of electrons resulting from He* atoms releasing their large internal energy when they collide with the MCP surface. Then the electrons are accelerated towards the PS (Phosphor Screen) biased at positive 2000V and cause fluorescence of the phosphor at the place of impact, thus allowing for position sensitive measurements of the He* atoms. The brightness is roughly proportional to the flux of the electrons, which is also proportional to the number of incoming He* atoms. It should be noted that the detector system responds to both the He* atoms and the UV light from the source discharge in the same say so that the image on the detector is always composed of two parts: the bright vertical line is the slit image from the UV light, and the smeared out grey part to the left of the line is the image of the pushed He* atoms, as can be seen from FIG. 3.6.

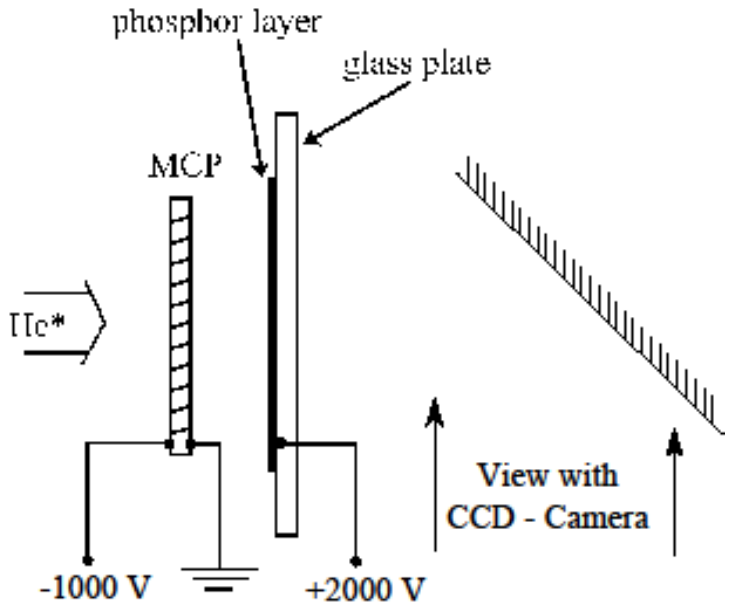

FIG.3.5: Schematic of the MCP/PS detector for He* beam detection. The mirror was mounted at 45 degrees in order to reflect the image through the side window of the vacuum chamber. Images of the screen are taken by a CCD camera. Ref. [27].

In the current experiment the phosphor screen was self-made following the procedures outlined in Ref.[30]. With the sedimentation process, the phosphor can be uniformly applied to the ITO coated glass, and one can just use a cotton swab to remove the phosphor around the margin of the glass and apply the copper tape in order to make electrical connection with the metal plates sandwiching the phosphor screen. The whole process takes about 3 days, and it provides us with an inexpensive alternative compared with a commercial LEXEL Imaging PS that costs around $1K and about 5 weeks lead time.

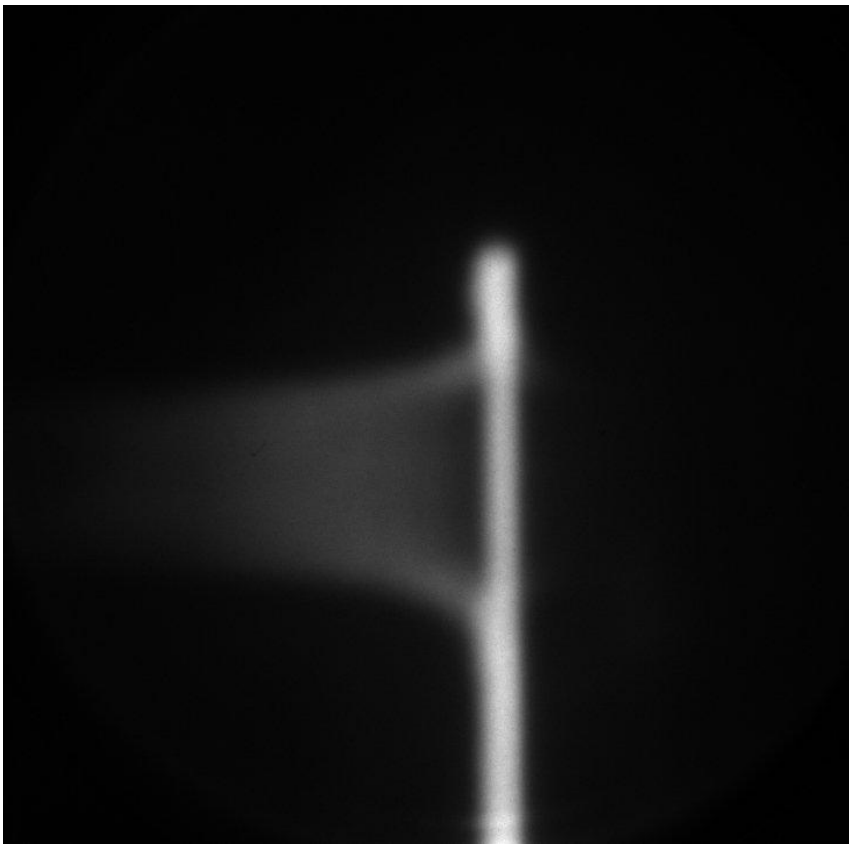

FIG.3.6: camera image of the phosphor screen with the slit and deflected atoms. The bright line is the slit image and the atoms are pushed to the left. [25]

3.3 ARP Light Production

This section describes the optical system in the ARP experiment. There are mainly three stages in producing the ARP light: the production of the infrared light source and its frequency stabilization, the modulation to generate the ARP light pulse with a certain intensity envelop and frequency chirp, and the amplification of the ARP light pulse to reach the desired peak Rabi Frequency.

Laser:

The laser system consists of three DL 100 lasers from Toptica and the schematic of the laser cavity is shown in FIG. 3.7. The extended cavity is in Littrow configuration, and the zeroth order refection serves as the output. The frequency of the output can be coarsely tuned by changing the angle of the diffraction grating via manual control of a screw set, or finely controlled by a piezo-electric transducer (PZT) mounted behind the diffraction grating. The output after leaving the extended cavity is shaped by a fiber coupling collimation lens and a pair of anamorphic prisms and finally enters an optical fiber via a Toptica FiberDock^{TM}, which is oriented in a way to make sure the polarization of the outgoing light is aligned to the slow axis of the polarization maintaining (PM) fibers. It should be noted here all fibers/fiber splitters between lasers and electro-optic modulators should be PM type since the incoming polarization always needs to be aligned with the fast axis of the crystal in the electro-optic modulator or the power loss through it can be huge.

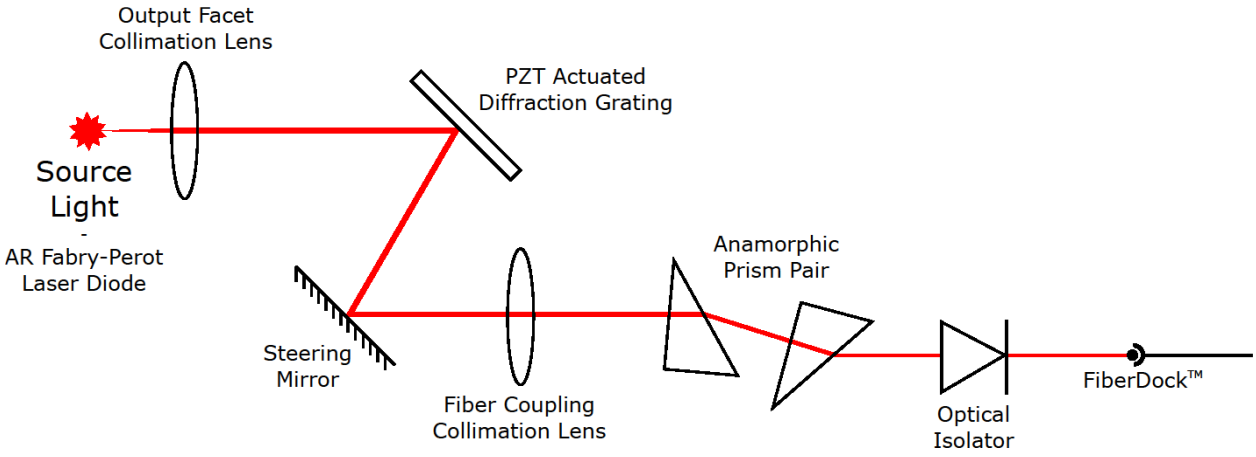

FIG.3.7: The Littrow configuration extended cavity of Toptica DL 100 laser from Ref [18].

From the block diagram of the major optical components, FIG. 3.8, one of the three lasers is frequency-locked via Saturation Absorption Spectroscopy (SAS) to the He* resonance and is called the master laser, while the other two can be either phase locked to the master laser or kept free-running and are called slave lasers. Here the phase lock refers to imparting a shared coherence between two lasers (i.e., master and slave), so that there is a stable frequency and phase difference between them [18]. The phase lock scheme was originally implemented to address the question of whether the coherence of the two light fields had an impact on the ARP force. In the present experiment, however, the phase lock is not used since previous data in Ref [18] has shown that the shape of the force profiles (to be discussed in Chapter 4, results) were nearly the same with or without the phase lock [18].

FIG. 3.8 also shows how the atomic velocity is simulated through the Doppler shift by oppositely detuning the counter-propagating optical pulses and the idea is as follows: the “beat measurement” block refers to mixing the frequency of the slave and master laser by a 50/50 fiber splitter and then inputting it into a fast photodiode which reads the beat frequency, i.e., detuning

of the slave laser from the master laser. The amount of detuning can be adjusted by tuning the scan control (SC110 Toptica) nob on the slave laser control rack, thus changing the Doppler shift velocity via the relation $kv = \delta$.

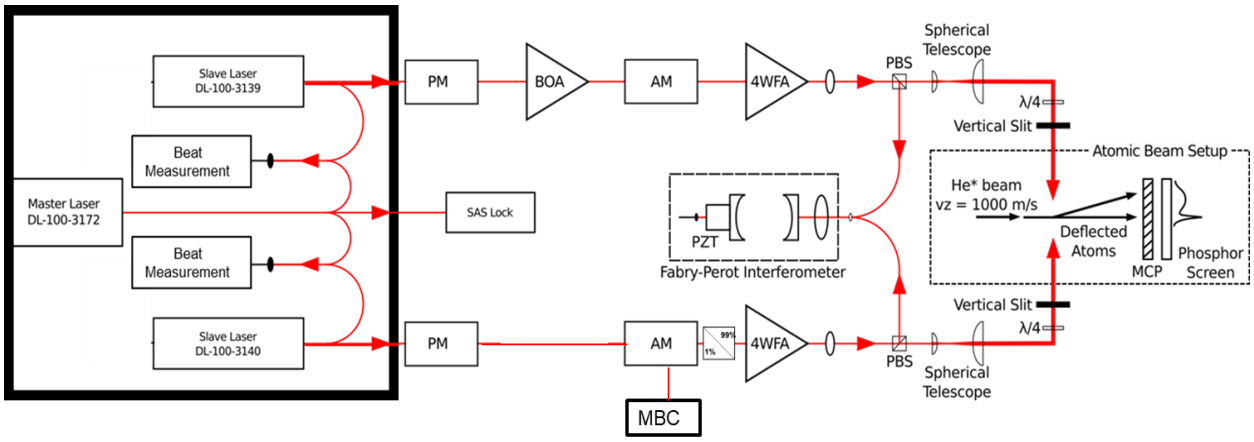

FIG.3.8: Major optical components in the experiment. PM-Phase Modulator, BOA-Booster Optical Amplifier, AM-Amplitude Modulator, 4WFA- 4 Watt Fiber Amplifier, SAS-Saturated Absorption Spectroscopy, MBC-Modulator Bias Controller, $\boldsymbol{\lambda/4}$- Quarter Wave Plate, MCP-Multi Channel Plate. Diagram adapted from Ref [31].

Electro-optic Modulators and Modulator Bias Controller:

As we discussed in Chapter 2, ARP theory, the ARP pulse is tailored to have a half-sinusoidal pulse shape and a specific frequency chirp within the pulse. To this end, electro-optical modulators (EOM) are used which utilizes the linear electro-optical effect in a $LiNbO_3$ crystal, that is, the index of refraction of the $LiNbO_3$ changes proportionally to the varying applied electric field, thus introducing a time dependent phase delay to the light passing through the EOM. Two

types of EOMs are used in generating the ARP pulse and are called phase modulator and amplitude modulator. This section describes the phase modulator (PM) for the frequency chirp generation followed by the amplitude modulator (AM) for the pulse generation. Then, it moves to discuss about the modulator bias controller, which controls the bias voltage across the amplitude modulator and corrects for the voltage drifts that cause poor optical pulse quality.

Phase Modulator:

The schematic of a phase modulator is given in FIG. 3.9. The optical field after passing through the PM with a phase delay resulting from a sinusoidal rf signal applied to the phase modulator has the form of:

$$E(t) = E_0 \cos(\omega_l t - \beta \, sin(\omega_m t)) \tag{3.1}$$

Where E_0 is the light field amplitude, ω_l and ω_m are the unmodulated light frequency and rf modulation frequency respectively, and β is the modulation index, which is related to the physical parameters of the modulator and can be measured experimentally. Details of this measurement can be found in previous theses [23]. The instantaneous frequency is given then by taking the time derivative of the overall phase of the light field, that is,

$$\omega(t) = \frac{d\phi(t)}{dt} = \omega_l - \beta\omega_m \cos(\omega_m t) \tag{3.2}$$

In this way the cosinusoidal frequency chirp at a modulation frequency of ω_m described in Chapter 2 is achieved with a sinusoidal rf signal at the PM.

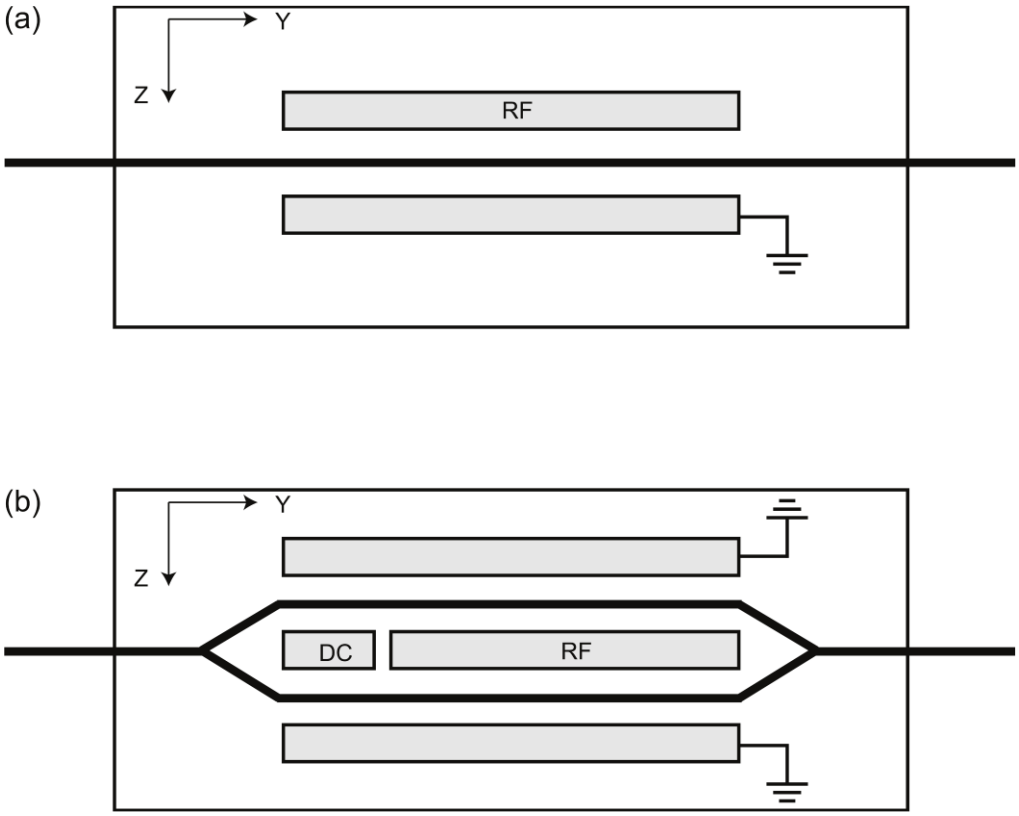

FIG.3.9: Schematic layouts of (a) phase modulator and (b) amplitude modulator. Both upper left corners show the principal axes of the $LiNbO_3$ crystal, from Ref [25].

Amplitude Modulator:

The schematic of an amplitude modulator is given in FIG. 3.9 (b). It consists of two $LiNbO_3$ based waveguides in the Mach-Zehnder interferometer configuration, and the incoming light is first split into two paths and then recombined. Two central electrodes are connected to a DC power supply and a rf signal source respectively while the outer surfaces of two waveguides are grounded.

When applying a voltage to the central electrodes, each path experiences an electric field of equal magnitude but of opposite directions, which means that the optical fields through the two paths experience opposite shifts, $\pm\phi$ and the output electric field can be written as:

$$E(t) = \frac{E_0}{2}[\sin(\omega_l t + \phi) + \sin(\omega_l t - \phi)] = E_0 sin\phi \sin(\omega_l t) \tag{3.3}$$

The DC voltage is set to a value to cause total destructive interference without the presence of the rf signal, and the rf signal induces a time varying phase change $\pm\phi(t)$ so that the resulting output power is:

$$P(t) = \frac{P_0}{2}[1 + sin2\phi(t)] \tag{3.4}$$

Where P_0 is the maximum output power. FIG. 3.10 is the plot of output power from an amplitude modulator for a given voltage and there are four common operating points, i.e., MIN, MAX, Quad- and Quad+. In the current experiment, the DC bias is kept at the MIN point in order to create total destructive interference while the rf signal with its peak voltage of V_π intermittently creates total constructive interference resulting in an optical pulse. Chapter 2 shows that the ARP pulse in the current experiment has a half sine shape at 25% duty cycle, and this is done by operating the signal generator that produces the rf signal at 320 MHz with ¼ pulse rate and 17% duty cycle. The measured optical pulse train with 80 MHz repetition rate can be seen in FIG. 3.11.

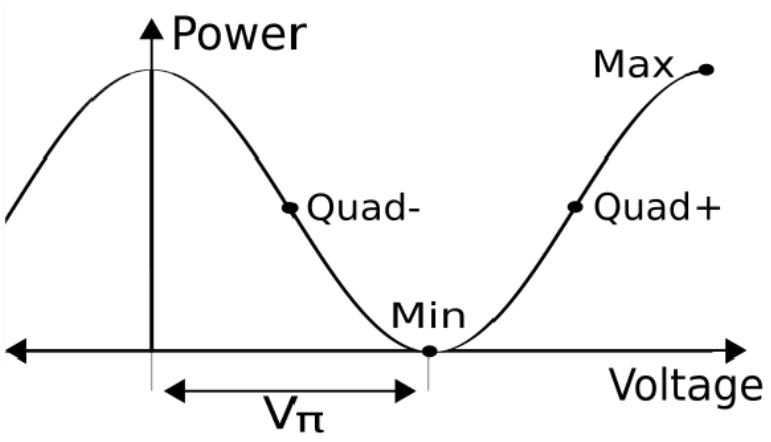

FIG.3.10: Plot of optical power from AM versus DC bias voltage. When DC voltage is set at MIN and the rf signal intermittently applies $\boldsymbol{V_\pi}$ so that the power reaches to MAX. This process creates a pulse. Picture adapted from Ref [32].

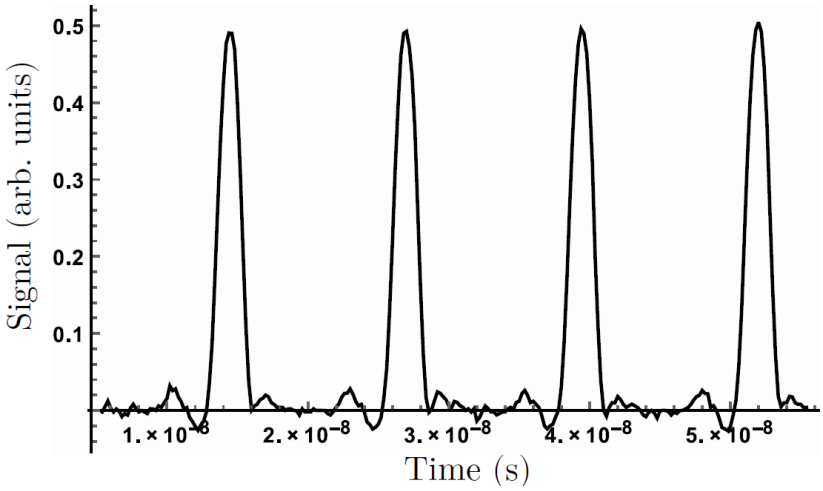

FIG.3.11: Oscilloscope image of the periodic optical pulse delivered by the AM. The repetition rate is 80 MHz and the pulse width is about 3.125 ns measured from the baseline, from Ref [25].

Charactering the ARP light pulse requires monitoring the spectrum in both time and frequency frame. FIG. 3.12 shows the ideal Fabry-Perot spectrum of an amplitude modulated light pulse, which can be seen as the Fourier transform of FIG. 3.11. These peaks are 80 MHz apart, and theoretically the height of each frequency component is [23]:

$$I^{FP}(\omega_l + n\omega_m) = \left(\frac{4}{4-n^2}\right)^2 cos^2\frac{n\pi}{4} \tag{3.5}$$

The amplitude of the central peak has been shown to be extremely sensitive to a small change in the DC bias voltage [23] as can be seen in FIG. 3.13 and the shape of the Fabry-Perot spectrum needs to be monitored during the experiment to ensure proper ARP pulse production.

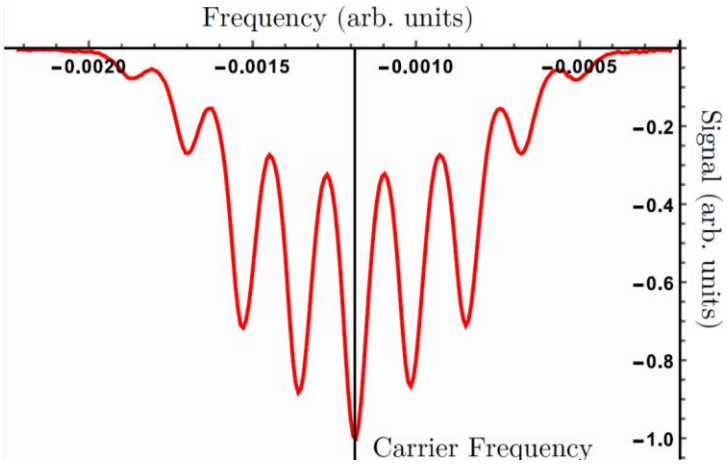

FIG.3. 12: A Fabry-Perot spectrum of the amplitude modulated (only) light pulse.

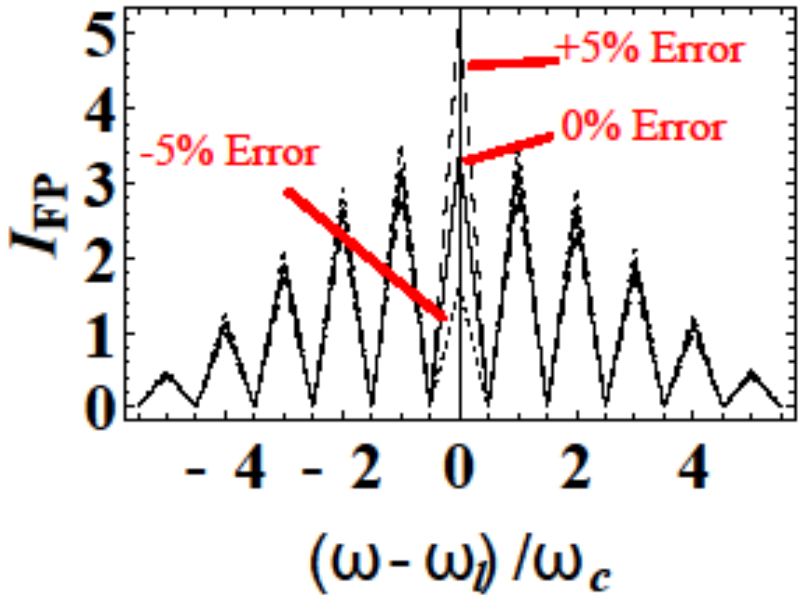

FIG.3.13: The theoretical amplitude modulated pulse shape. The Fabry-Perot spectrum is a convenient way to monitor the DC bias voltage drift since the central peak is very sensitive to the DC voltage change via other peaks are insensitive, from Ref[27].

Modulator Bias Controller:

As stated in the previous section, the ideal DC bias voltage is set at the MIN operating point to create a total destructive interference. However, for the traditional Mach-Zehnder interferometer, a small change in the path length of two arms due to thermal expansion or contraction can negatively affect the end interference, resulting in a drift in the operating point, which lowers the power of the pulse and induces residual light during the dead time, which can be seen in the central peak of the Fabry-Perot spectrum deviating from its ideal height. These drifts occur in minutes and the previous solution to manually adjust the DC power whenever the central peak height changes required near constant attention, and often required multiple tries in taking one data point.

In order to stabilize the DC bias voltage, preferably in an automated way, a modulator bias controller (MBC) has been built by Ian Schwartz for his MSI project. FIG. 3.14 is a schematic of the MBC electronics. Details of the MBC can be found in Ian's thesis and won't be repeated here. An overview of his idea is that one can use a small portion of the amplitude modulator output as an error signal for a PID controller, and the algorithm can correct the input voltage whenever the light power changes (during the deadtime).

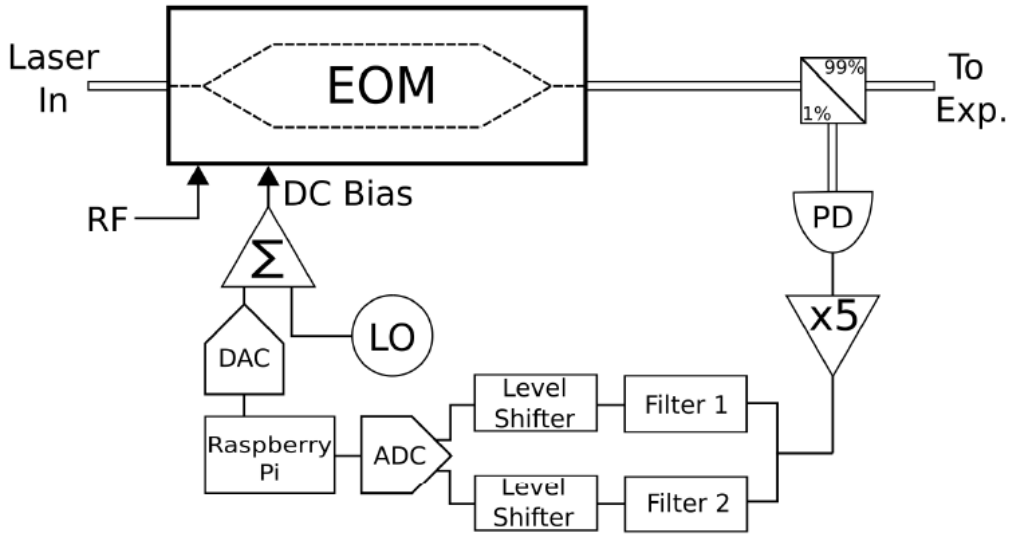

FIG.3.14: Block diagram of the modulator controller. PD-photodetector, X5- 5 times gain amplifier, ADC-analog-digital converter, DAC-digital-analog converter, LO-local oscillator, **Σ**-summing amplifier from Ref [32].

Fiber amplifiers and Booster Optical Amplifiers:

The ARP pulse generally requires about 1W average power and that is why amplifiers are needed at multiple stages along optical beam paths to account for insertion losses of both amplitude and phase modulators, power loss due to the ¼ pulse rate, and various kinds of other power loss in fiber splicing points and mating sleeves. There are two types of amplifiers used in the current experiment that are based on different gain mediums. The Keopsys model KPS-BT2-YFA 4W fiber amplifier (4WFA) and Optocom fiber amplifier uses Yb-doped fibers as a gain medium and the Booster Optical Amplifier (BOA) can be viewed as a single pass semiconductor diode laser with anti-reflective coatings on its faces. The BOA provides a small gain to the optical power to seed the 4WFA which requires an average input power larger than 0.5 mW in its pre-amp stage. FIG. 3.8 provides a block diagram of the optical beam path. It should be noted that in the current experiment, another kind of fiber amplifier Optocom has been implemented on both beam lines to compensate for the gain degradation of BOA over time.

Typically, the power before any modulation is around 25 mW, and it drops to about 7 mW after passing through the phase modulator. The BOA/Optocom between the phase modulator and amplitude modulator boosts the power to larger than 9 mW to ensure that the power out of the amplitude modulator, after more than 3/4 of the power loss due to pulsed beam generation and the power loss due to fiber splicing points between single mode (SM) fibers and polarization maintaining (PM) fibers, still exceeds the input threshold of 0.5 mW for the 4W fiber amplifier at the end of the beam line.

One important consideration in operating the amplifiers is avoiding the unwanted amplified spontaneous emission (ASE). ASE is light, produced by spontaneous emission, that has been optically pumped by the process of stimulated emission in a gain medium. It not only generates incoherent light, but also limits the maximum gain that can be achieved in the gain medium,

resulting in an ARP pulse with improper power and unwanted frequency components from incoherent light. FIG. 3.15 is the frequency spectrums of amplified light with ASE taken by an Ocean Optics Spectrometer. The peak near the end of the spectrums is He* resonance frequency, while the small bump on the left of the He* peak in FIG. 3.15 shows frequency components due to ASE. The main reason for ASE occurrence in the current experiment is when there is not enough light seeding the amplifier. In order to monitor the power, there are several checkpoints connected by fiber mating sleeves along the optical path to make sure the light power entering the Optocom is higher than around 1 mW and that going into 4WFA higher than 0.5 mW.

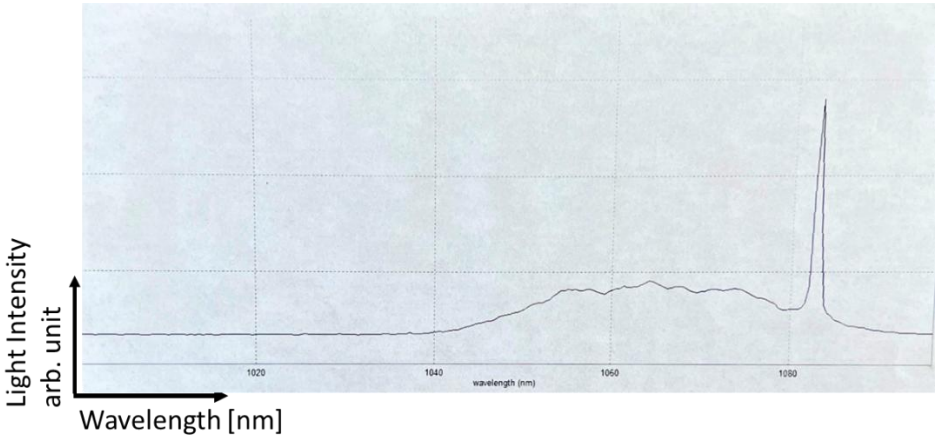

FIG.3.15: ASE spectrum after the 4WFA taken by a spectrometer. The strong peak at the right end of the figure is the resonance He* frequency @ 1083.33 nm and the bump to its left represents the frequency spectrum of ASE and its wavelength spans from 1040 nm to 1080 nm.

Production of the ARP light:

An ARP pulse requires both a frequency sweep and an amplitude modulation that are aligned in time, as is shown in the frequency spectrum of the chirped and pulsed ARP light in FIG. 3.16 (a) by the Fabry-Perot. Details about the expected Fabry-Perot spectrum for the ARP pulse can be found in Ref [25]. and the criteria used in the current experiment to determine whether the chirp properly aligns with the pulse is to see whether the spectrum is symmetric. For a chirp that is out of phase with the pulse, the spectrum is skewed in one direction or the other (see FIG. 3.16 (b)).

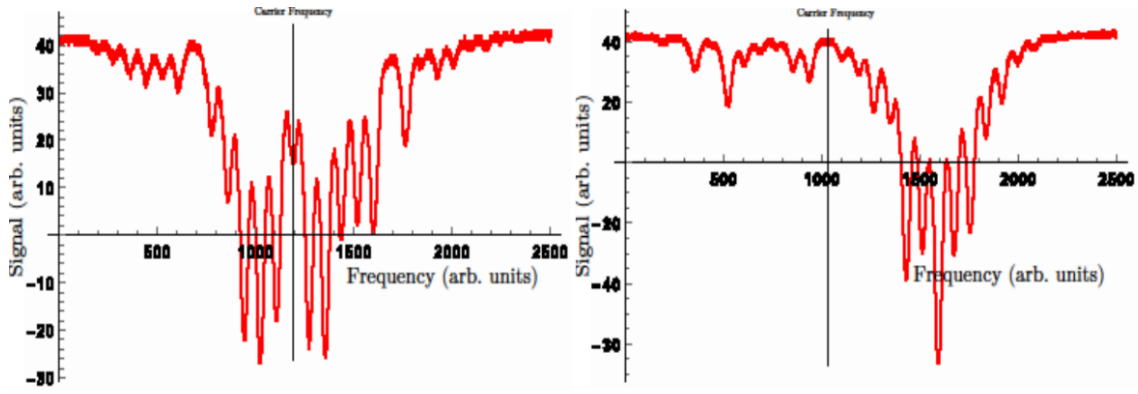

(a) Properly aligned AM+PM pulse (b) Misaligned AM+PM pulse

FIG.3.16: Illustration of a properly aligned phase modulated and amplitude modulated pulse vs a misaligned one, from Ref [27].

Data Analysis:

FIG.3.17 shows an image of the phosphor screen with deflected atoms. It's taken from [25] and is used here to demonstrate the data collection and analysis process. For each frame of MCP/PS images (corresponding to each simulated Doppler velocity of atoms), a narrow region at the center of the pushed atoms (about 10 pixels in width) is cropped (denoted by a red rectangle in the right figure) as the area of interest since the intensity near the center of the Gaussian beam can be approximated as being uniform. The blue curve in the left figure shows the averaged intensity over each row of pixels and is often referred to as lineouts, and the red curve on top of it is the Gaussian fitting for both the background slit and pushed atoms, which usually provides an accurate fit of the lineout, or sometimes, a Maxwellian profile is used to fit the shape of the deflected atoms, which better mimics the longitudinal velocity profile of the atoms [18]. In the present experiment, the pushed peak in FIG. 3.18 is much larger and wider compared with the previous data, which means more atoms interact with the ARP light and are pushed away from the slit. This higher efficiency of He* atom production is probably a result of new parameter settings of discharge voltage and inlet pressures (refer to Section 3.1 for details). The present lineouts in FIG. 3.18 clearly won't fit well with two Gaussian profiles and there is still an ongoing discussion about how to better estimate the centroid position of the pushed peak and its associated error bar. For right now, the preliminary analysis method is as follows: for determining the centroid position, we first identify a region containing the maximum intensity position and adjacent data points (about 30-50 points to the left and right of the MAX point), and then fit a Gaussian profile to this region to get the centroid position. As for the error bar, we define it as the range within which the data points are higher than 95% of the maximum intensity. The centroid plots shown in Chapter 4 are based on the above analysis method.

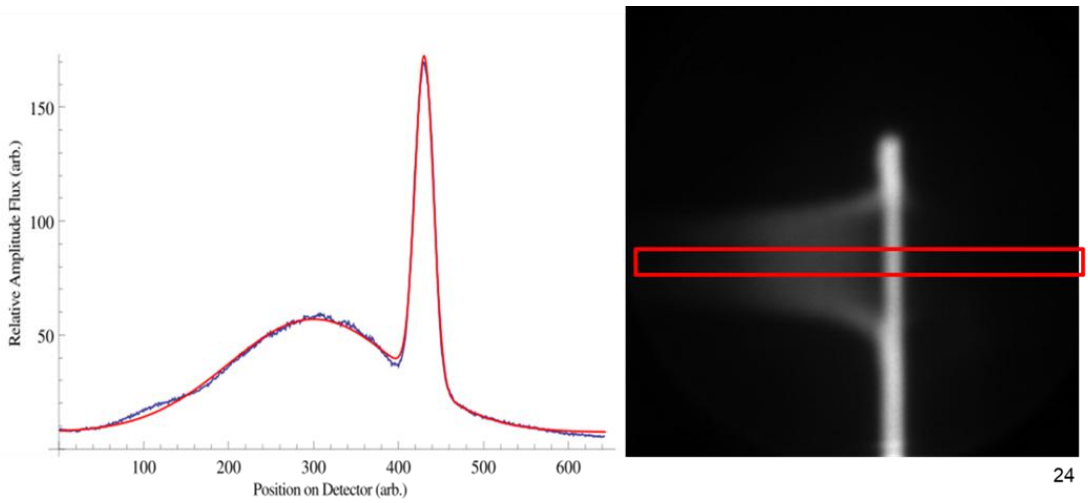

FIG.3.17 Image of the phosphor screen showing deflected atoms and the lineout with the fitting of the area of interest. Adapted from Ref [25].

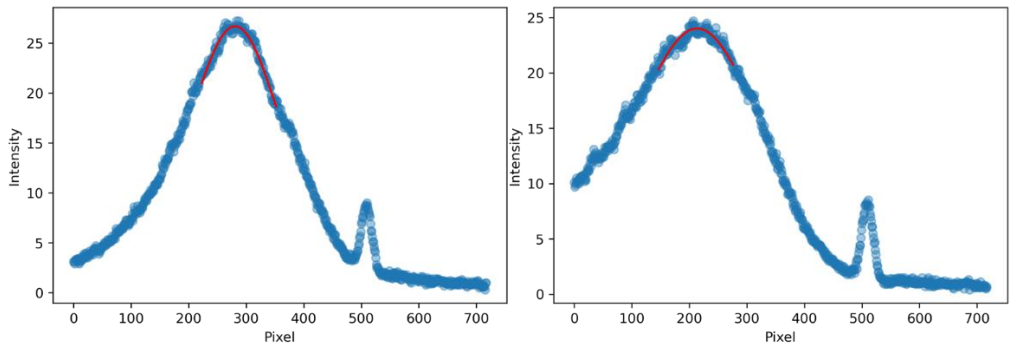

FIG.3.18: Two sample images of lineouts from the present data. The x-axis is the pixel number on the phosphor screen and the y-axis is a dimensionless number representing the density of atoms. The blue curve is the actual data and the red curve on top of it is the Gaussian fit.

Chapter 4: Results

This chapter begins with a review of previous simulation efforts in the exploration of the ARP force (Section 4.1). Then, it proceeds to present the current experimental data followed by a discussion focused on unexpected observations in the present data based on a comparison between the previous simulation and the current experiment (Section 4.2 and 4.3). Next, the section presents the limitations of the present experimental set up and provides an outlook for future upgrades (Section 4.4). Last, the section concludes with a summary of the present work. (Section 4.5)

4.1 Previous simulation results

Previous simulations from Ref [27]. studied the roles of sweep directions on the force vs velocity profile. It has been demonstrated by the contour plots of the average force calculated over a range of the experimental parameters Ω_0/ω_m and δ_0/ω_m in Ref [27] FIG. 2.3 that, the magnitude of the force is independent of sweep directions for on-resonance atoms (zero velocity). In contrast, as has been shown in Ref [27] FIG. 2.8, the simulated force profiles for non-zero velocities seem to depend on the sweep directions, with an asymmetry around zero velocity when two consecutive sweeps are in the same direction (Up-Up or Down-Down), and a symmetry around zero velocity when two consecutive sweeps are in different directions (Up-Down or Down-Up).

It should be pointed out that the previous simulations by Ref [27] are based on a "dragged atom approach" [19]. Specifically, velocities of atoms moving under the "dragged atom approach" along the axis of the propagating ARP pulses (e.g. transverse velocity) are fixed, leading to constant Doppler shifts $\pm kv$ of atoms during the entire time of interaction with ARP pulses. However, as pointed out by later studies [25], the "dragged atom approach" is a good

approximation only when it is used to calculate radiative force or forces of a similar magnitude over a short interaction time, the reason being that the velocity change caused by these forces would result in a Doppler shift typically smaller than or comparable to the natural linewidth γ of the atomic transition. However, it is not the case for the ARP force. In fact, during an interaction time of about 320 pulse pairs, the cumulative Doppler shift δ_{max} turns out to be much larger than the natural linewidth γ, as shown by $\delta_{max} \approx 2\pi * 54\ \text{MHz} \gg\ \gamma = 2\pi * 1.62\ \text{MHz}$ in eq. 5.7 of Ref [25]. To account for the moving atom, the updated simulation code by Ref[25]. changes the value of atom's transverse velocity after interacting with each ARP pulse pair. It should be noted that the updated simulation not only changes atom's velocity during the interaction time, but also changes the relative phase differences ϕ_{rel} between the two ARP pulses, as illustrated in eq. 5.9 of Ref [25].

FIG. 4.1 which is reproduced from FIG. 5.3 of Ref [25], compared the force vs velocity plots between the "dragged atom approach" and the "moving atom approach" described above for the Up-Up sweep direction. As pointed out by Ref [25], there are mainly three new features emerging from the moving atom approach: the disappearance of narrow resonance peaks, the "oscillating" peaks at higher velocities, and the shift of the central peak away from the zero velocity.

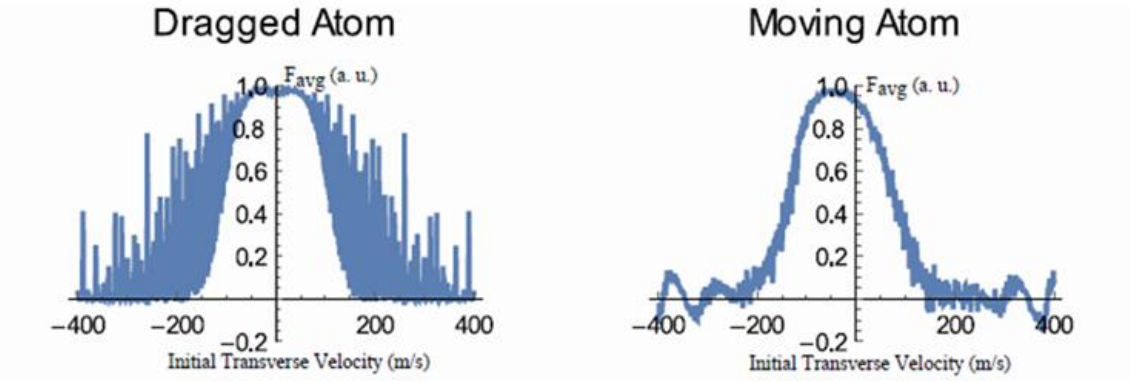

FIG.4.1: Force vs. velocity plots at ($\boldsymbol{\Omega_0/\omega_m}$, $\boldsymbol{\delta_0/\omega_m}$) = (3.37, 4.11) for both the dragged atom picture and the moving atom picture. (Figure adapted from Ref [25])

4.2 ARP for different sweep directions

This section and the following section present the experimental results of the present thesis. In this section, the experimental data of force vs. velocity plots for various sweep direction combinations are presented and are compared with the simulated force vs. velocity plots based on the "moving atom approach".

During experiments, the ARP force is measured as a function of atomic velocity across all sweep direction combinations (Up-Up, Down-Down, Up-Down, Down-Up) with an expanded velocity range ({-500, +500} m/s, while the previous range was {-300, +300} m/s). Rabi frequency Ω_0 and frequency sweep range δ_0 were chosen to be ($3.38\ \omega_{m,}$4.94 ω_m), which was measured to be the optimal force parameter set in Ref [18] and were not accessible experimentally in the previous force profile measurement.

FIG. 4.2 and 4.3 show the measured velocity dependence on ARP force for all four sweep direction combinations. The x-axis of these plots is simulated velocity, which is related to the Doppler detuning δ of the laser by $\delta = kv$. The step size in our data taking is $\Delta\delta = 20$ MHz, and the error bar of around ± 8 MHz is caused by drifts of the scan control unit in the TOPTICA laser control system. The y-axis values are the pushed distances that the deflected atoms travel after interacting with the ARP light field, which is proportional to the magnitude of the ARP force. The y-axis values are scaled by the pushed distance of the radiative force d_{rad}. d_{rad} represents the pushed distance of the atoms from the slit (at position zero) by a radiative force. d_{rad} is measured at the beginning of each data run (during a data run, 50 pushed distance data corresponding to 50

simulated atomic velocities for a specific sweep direction combination are measured) for calibration purposes among different data runs.

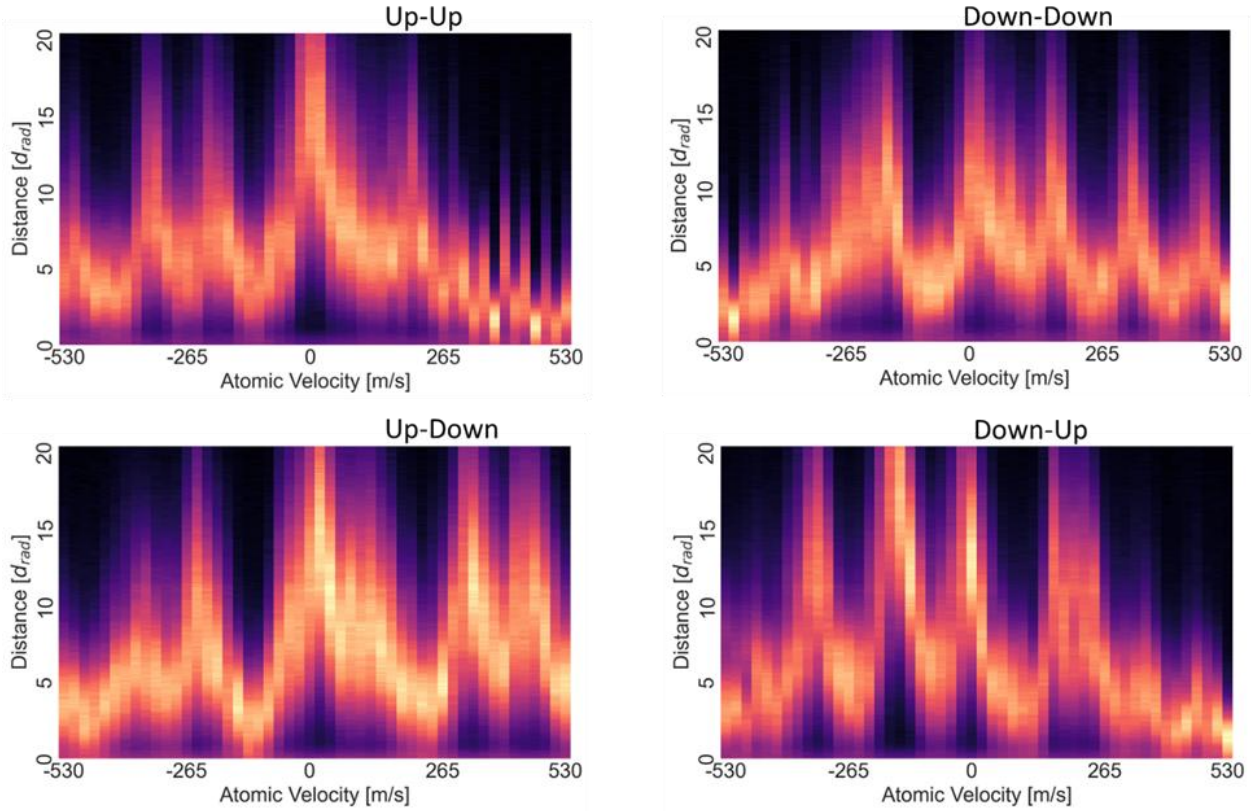

FIG.4. 2: ARP pushed distances vs. velocity plots for all four sweep direction combinations.

For FIG. 4.2, These “force” vs. velocity plots come from rotating each line-out plot by 90 degrees clockwise and plotting the line-out plots in Chapter 3, FIG. 3.18, for each velocity bin, side by side. Thus, the aggregated plot represents atomic displacements by ARP for different velocities, with larger displacement going in an upward direction in the plot. In particular, different

colors in the plot represent different atomic density and the vertical spread of it depends on atom's longitudinal velocity distribution. Due to atoms' longitudinal velocity distribution, atoms with the same transverse velocity arrive at the downstream detector at different positions, resulting in wide spreads in the vertical columns. Therefore, the vertical spread is NOT noise. The UV background peak acts as a baseline of zero deflection but is barely seen in FIG. 4.2 since it is hidden just below the bottom of the figure.

One prominent feature of all the four force vs. velocity plots in FIG. 4.2 is the discrete peaks and valley structure. It is seen that there are strong upward peaks that are uniformly spaced along the velocity axis. This contradicts the previous simulation of the force profile, e.g., shown in FIG. 4.1, in which an overall force profile shows a maximum force centered around zero velocity and decreases smoothly with increasing velocities.

There had been speculations that these peak and valley structures could come from some systematic errors during the data taking processes. However, repeated measurements over months with different data acquisition methods continued to yield consistent force profiles, indicating that the peaks and valley structures are not a mere artifact, but a distinct feature of the ARP force vs velocity profile. In fact, the data for each figure in FIG. 4.2 were taken multiple times on different days over a time period of several weeks, in order to confirm the consistency of the peak positions and other structures. A more detailed discussion on the peak is given in Section 4.3.

It should be noted that, in the Up-Up sweep direction plot in FIG. 4.2, there seems to be a number of small, fast oscillating peaks emerging between 300 m/s and 500 m/s. Multiple data runs focusing on this velocity range have confirmed that these oscillating peaks are not artifacts, however, the nature of these peaks is still unclear.

The line plots of FIG. 4.3 present a different way to visualize the force vs. velocity plots in FIG. 4.2. They come from extracting the mean and variance from the fitted peaks of the same data and offer a clearer view of both the overall shape of the force profiles and the peaks and valley structures. Although the peak heights and positions vary among force profiles of different sweep direction combinations, there are two common features for all four plots: First, the overall force profile are maximized at around zero velocity and decrease with larger velocities. Second, the peak-to-peak spacings are approximately between 150 m/s and 200 m/s (see Section 4.3 for discussions on the peak spacings).

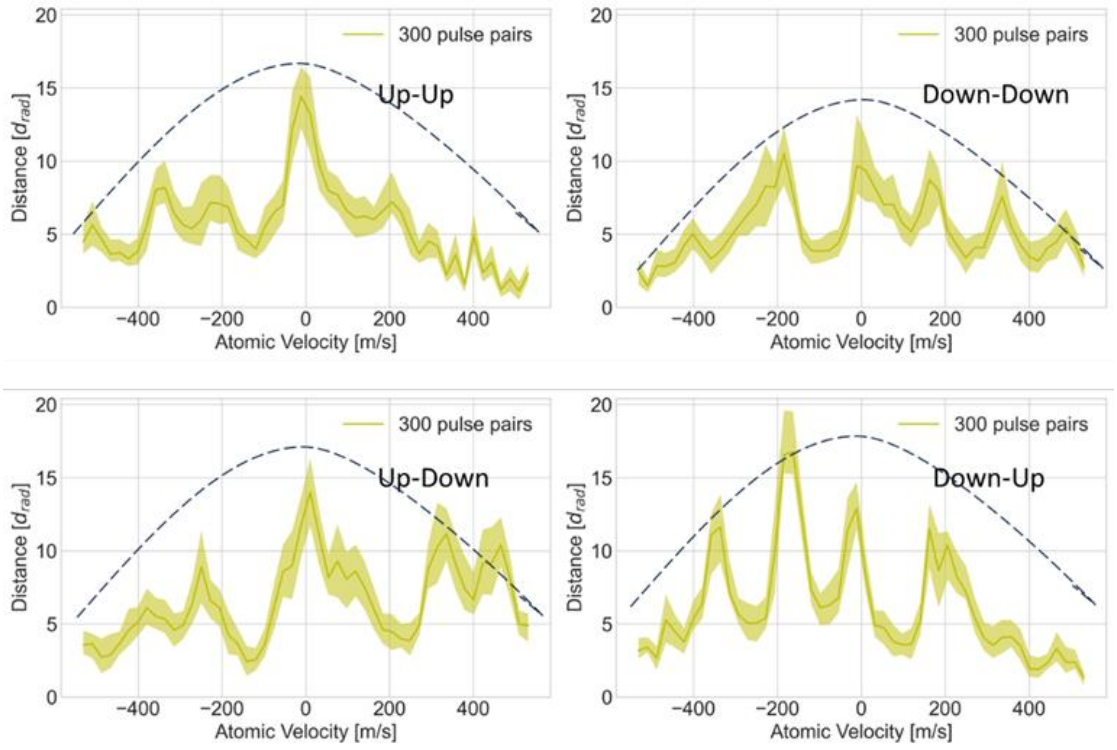

FIG.4.3: Line plots of the force vs velocity plots for all four sweep direction combinations.

Despite the above two common features for the four force profiles, it's clear that both the peak positions and peak heights are different for different sweep direction combinations. From the discussion on [27] simulation result in Section 4.1, the force vs. velocity plots are asymmetric with respect to the velocity reversal when consecutive pulses sweep in the same direction (up-up or down-down case), while down-up and up-down cases are symmetric about zero velocity. However, the experimental force vs. velocity plots illustrated in FIG. 4.2 and FIG. 4.3 are inconsistent with the simulated results. As seen in FIG. 4.2 and FIG. 4.3, from left to right, all the force vs. velocity profiles show an approximate symmetry about zero velocity for the central peaks (spanning between -100 m/s to +100 m/s) and the overall force profiles (indicated by dashed lines).

Further, the experimental data is compared with the updated simulation from [25], illustrated in FIG. 4.1. Comparing the three features pointed out by [25], on one hand, these three features match qualitatively with the experimental plots, particularly the "oscillating" peaks at higher velocities and the off-centered central peak. On the other hand, there are still large discrepancies between the simulation and experimental results. Firstly, the central peak in the experimental force vs. velocity plots spans a narrower range compared to that of the simulation. Specifically, for all sweep directions, the central peaks span roughly between $-100\ m/s$ and $+100\ m/s$ for experimental plots, whereas the central peak in the simulation spans roughly between $-200\ m/s$ and $+200\ m/s$. Secondly, the "oscillating peaks" at higher velocities, or more accurately speaking, peaks at regularly spaced velocity intervals, in the experimental force vs. velocity plots shows a more prominent periodicity compared to that of the simulation. A more detailed analysis of these peaks in the experiment will be presented in section 4.3.

4.3 ARP for different interaction time

One path forward to study the velocity dependence on the ARP force is to look at forces at significantly shorter interaction times, as pointed out by [18], since it would help to better understand the fidelity or repeatability of the inversion from each ARP pulse pair if ARP force from fewer pulse pairs is compared with that from more pulse pairs. Therefore, varying widths of the light beams of 1.25 mm, 2.5 mm and 3.73 mm have been chosen as slit widths during experiment, which correspond to 100, 200 and 300 pulse pairs [33], respectively. All the data were taken on different days over a period of several weeks, during which the experimental setup, such as beam collimation lines, inevitably changes slightly from one data run to the other. Nonetheless, the velocity resonant peaks still show up clearly and are all quite similar for different pulse pairs and a given sweep direction combination, as can be seen in these 12 protocols in FIG. 4.4. It can also be seen that these peaks appear over a range of interaction times with about the same spacing and widths, and peak heights are typically twice as high as the average force in the region between them.

The appearances of periodic large peaks compared with the simulated ARP force magnitudes seems to indicate that there are coherence effects that have not been taken into account in the previous ARP description discussed in Chapter 2. Our current speculation is that the coherence might arise from atoms which moved exactly an integer number of wavelengths during the interaction between a first pulse pair and a second pulse pair, such that these atoms always see the same pulse to pulse phase ϕ_{pp} during the entire interaction with the ARP light. In contrast, atoms with different initial transverse velocities generally tend to encounter a pulse pair at different places, resulting in different phases ϕ_{pp} for each interaction. For example, an atom moving transversely at 100 m/s for 6.25 ns travels more than 600 nm during this time, and that's more than

one half wavelength. Since, during a multiple ARP pulses interaction, it's important that the motion of the Bloch vector is not discontinuously interrupted by any sharp phase changes[33], only atoms that move integer number of wavelengths would experience the same ϕ_{pp} that leads to consistently larger force compared with other atoms.

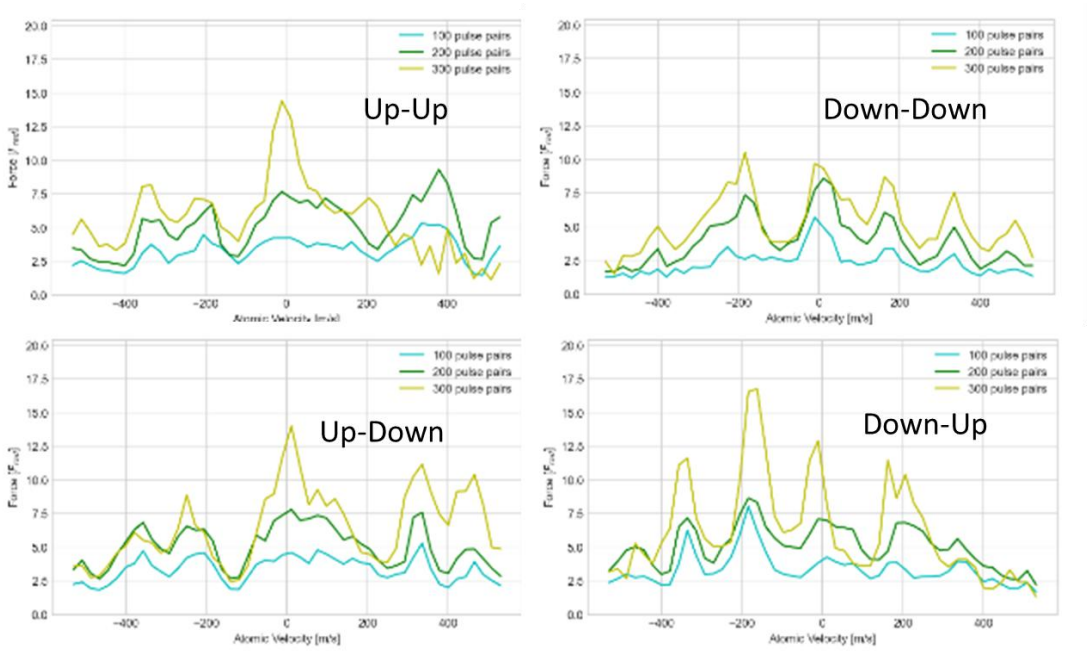

FIG.4.4: Force vs velocity line plots for different sweep direction combinations and different pulse number pairs.

To better visualize the periodicity of these velocity resonant peaks, peak spacings across all sweep direction combinations and pulse pair numbers are summarized in FIG. 4.5. It is clear that the peak spacing is centered around a velocity between $150\ m/s$ to $200\ m/s$. To further quantify the peak spacing, the peak spacings of the Down-Up sweep directions for all three pulse pair numbers are Fourier transformed and averaged, with the horizontal axis of $1/v_a$^2

transformed to v_a [33]. It can be seen from FIG. 4.6 that the Fourier transform peaks at $177 \pm 5\, m/s$. This result aligns with our preliminary view of ARP resonances discussed in the last paragraph. In particular, atoms that travel $v_a \times 6.25\, ns$ between pulse pairs that equals to $n\lambda$ yields $v_a = n \times 173\, m/s$. In this regard, our preliminary theory quantitively supports our experimental observation of peak spacings.

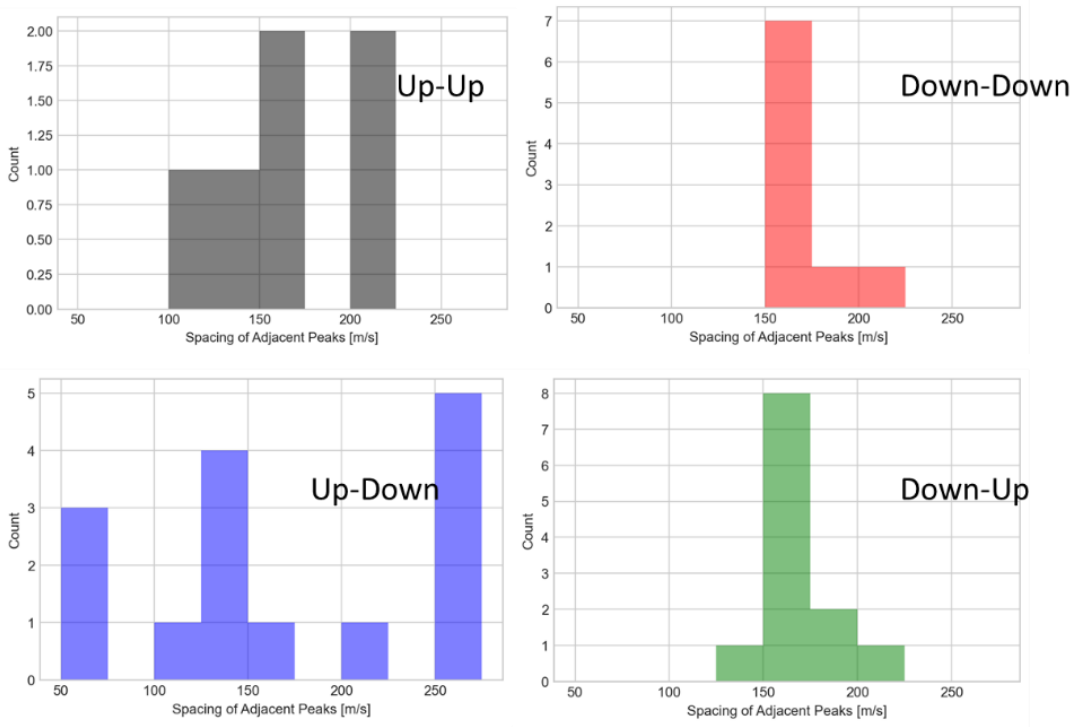

FIG.4.5: Spacing distributions of adjacent peaks for all pulse pairs and sweep direction combinations.

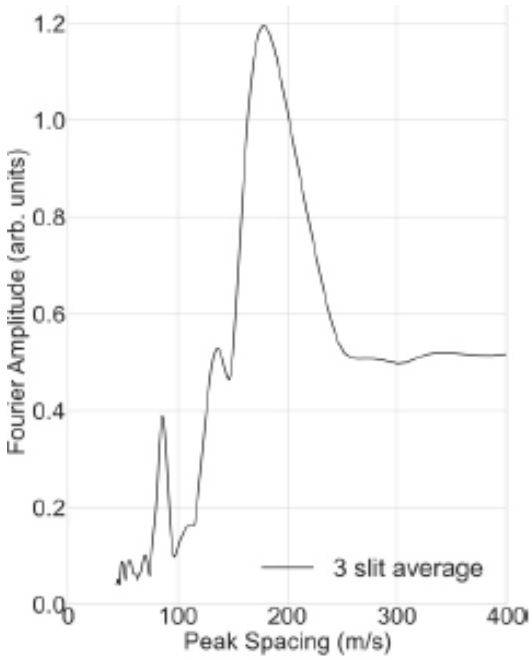

FIG.4.6: The Fourier transformed peak spacing distribution for all interaction times and sweep direction combinations.

4.4 Current limitations on the ARP force measurement and outlook

As presented in FIG. 4.2 – 4.4, the experimental ARP forces are measured with respect to the displacement of the atoms after their interaction with the ARP light field, as shown in FIG. 4.7. Specifically, there is a one-to-one correspondence between the displacement shown on the MCP + Phosphor Screen detector and the ARP force at a fixed longitudinal velocity of the atom. Another advantage of this setup is that the MCP + PS assembly is sensitive to the UV light emitted by the source, which is not deflected by the ARP light field and the image of which can be used as a baseline of atoms' displacement.

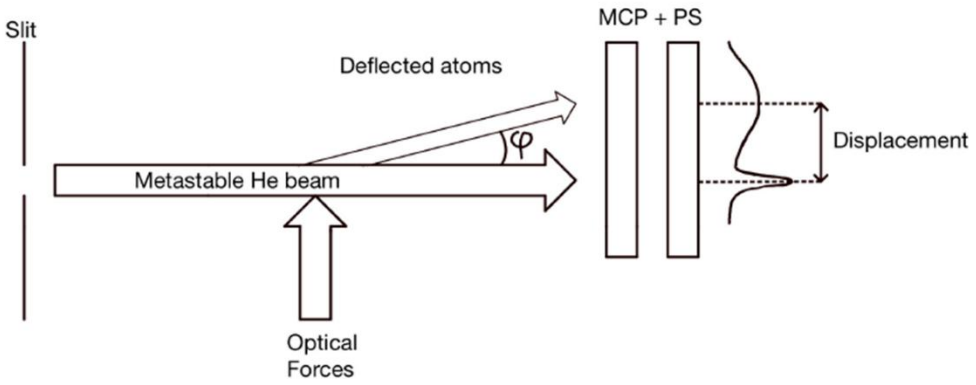

FIG.4.7: Present set up for indirectly measuring ARP forces based on atoms' displacement (picture adopted from Ref [34])

However, there are several limitations associated with this indirect way of ARP force measurement. Firstly, the distribution of longitudinal velocities v_l needs to be accounted for when using the MCP + PS assembly. Since atoms with different v_l spends different times interacting with the ARP light field, they acquire different amounts of transverse momentum that result in different displacements on the PS detector. Additionally, atoms with different v_l travel for different times from the interaction region to the detector, leading to further spreadings in their displacements on the PS detector. This is why the deflected atoms show a wide distribution of displacements shown in FIG. 3.18.

According to FIG. 3.18, for every simulated transverse velocity of atoms, the resulting transverse displacement spans a wide distribution. In the current data analysis, the distribution is approximated as a Gaussian distribution, and the "ARP force" is assigned to be the mean value of the Gaussian fit. However, it is not precise since the displacement distribution of atoms, in theory, is a complicated convolution of Lorentzian distribution and Gaussian distribution, and thus the mean value of the distribution is not an optimal approximation of the ARP force.

Further, the MCP + PS assembly is not sensitive enough, especially for smaller displacements. It is important, as stated in Section 4.3, to measure ARP forces for different number of pulse pairs to gain understanding of the repeatability of ARP sequences. However, for shorter pulse times, the displacements are smaller and difficult to discern on the PS screen. As an example, the left figure of FIG. 3.18 shows a smaller displacement of the deflected atoms compared with the right figure, and the smaller displacement results in a larger overlap with the UV slit distribution, making it more challenging to curve fit the displacement and retrieve the mean value.

To address the limitation of the current measurement scheme, there is an ongoing effort to directly measure the velocity distribution of deflected atom using a velocimetry detector based on the Doppler shift of the induced fluorescence of the light from an auxiliary laser. A detailed description of the detector and preliminary results are given in [34]. The basic idea is that the collected fluorescence signal would peak at a detuning $\delta = \vec{k} * \vec{v}$, with $\vec{v}$ being the transverse velocity of the atom, when sweeping the frequency of the light. With this direct measurement of velocity resulted from ARP interaction, the above problems of the current MCP + CP assembly can be resolved.

4.5 Conclusion

An essential characteristic of optical forces is their dependence on velocity. For laser cooling, forces need to be strong at specific velocities while diminishing at others, enabling the compression of atoms initially spread over a wide velocity range into a region where the force is zero. The effectiveness of these forces depends on both their range and strength within the region where they are non-zero.

The thesis presents an extensive study of the velocity dependence of the ARP force. Despite its ability to exert large forces on the atom, there remains many questions related to the structure

of the force vs. velocity profile. Specifically, the ARP force has been demonstrated to be around an order of magnitude larger than a radiative force. Moreover, the ARP force is also very effective over a much larger velocity range, spanning from $-500\ m/s$ to $+500\ m/s$. Surprisingly, large peaks in the magnitude of this force were observed at regularly spaced velocity intervals, suggesting the involvement of unexpected coherence effects in optical forces, including those used in laser cooling. Repeated measurements conducted over several months, using different data acquisition methods, consistently produced the same force profiles. This consistency suggests that the observed peaks and valleys are not mere artifacts, but rather a distinct feature of the ARP force versus velocity profile. To better understand how this force depends on various parameters, the velocity distributions of the atoms along the force direction were measured after the ARP interaction. This was done indirectly by measuring the displacement of the deflected atomic beam. A preliminary explanation related to phase relationships between atoms and ARP pulse pairs provides a quantitative explanation of the coherence effects.

It is also acknowledged that the current experimental setup limits the ability to measure small ARP forces and directly retrieve atomic velocities from position measurements. To address these limitations, new velocimetry detector is being developed to provide more easily interpretable results[34].

Bibliography

[1]. D. Wineland and H. Dehmelt. Bull. Am. Phys. Soc., 20:637, 1975.

[2]. T. Hansch and A. Schawlow. Op. Comm., 13(1):68-71, 1975.

[3]. D. Wineland and W. Itano. Phys. Rev. A, 20(4):1521-1540, 1979.

[4]. D. Wineland, R. Drullinger, and F. Walls. Phys. Rev. Lett., 40:1639-1642, 1978.

[5]. S. Andreev, V. Balykin, V. Letokhov, and V. Minogin. JETP, 34:442, 1981.

[6]. M.H. Anderson, J.R. Ensher, M.R. Matthews, C.E. Wieman, and E.A. Cornell. Science, 269(5221):198-201, 1995.

[7]. K. Davis, M-O. Mewes, M. Andrews, M. van Druten, D. Durfee, D. Kurn, and W. Ketterle. Phys. Rev. Lett., 75:3969, 1995.

[8]. Hänsch, T. W.; Schawlow, A. L. (January 1975). "Cooling of gases by laser radiation". Optics Communications. 13 (1): 68–69.

[9]. M. Williams, F. Chi, M. Cashen, and H. Metcalf. Phys. Rev. A, 60:R1763{R1766, 1999.

[10]. X. Miao, E. Wertz, M. G. Cohen, and H. Metcalf. Phys. Rev. A, 75:011402, 2007.

[11]. M A Chieda and E E Eyler. Prospects for rapid deceleration of small molecules by optical bichromatic forces. Physical Review A, 84(6):063401, 2011.

[12]. M.T. Hummon J.V. Porto A.M. Jayich, A.C. Vutha and W.C. Campbell. Continuous all-optical deceleration and single-photon cooling of molecular beams. Physical Review A, 89(2):023425, 2014.

[13]. H. Metcalf and P. van der Straten. Cooling and trapping of neutral atoms. 244(4-5):204-286, 1994.

[14]. C.J. Foot. Atomic Physics. Oxford University Press, New York, 2005.

[15]. L. Allen and J.H. Eberly. Optical Resonance and Two-Level Atoms. Dover, New York, 1987.

[16]. P. van der Straten and H. Metcalf. Atoms and Molecules Interacting with Light. *Cambridge University Press*, Cambridge, 2016

[17]. R. Feynman, F. Vernon, and R. Hellwarth. Geometrical representation of the Schrodinger equation for solving maser problems. *JOUAP*, 28(1):49-52, 1957.

[18]. B. Arnold. Velocity Dependence of the Adiabatic Rapid Passage Force in Metastable Helium. PhD thesis, Stony Brook University, 2019.

[19]. H. Metcalf and P. van der Straten. Laser Cooling and Trapping. *Springer*, New York, 1999.

[20]. A. Abragam. The Principles of Nuclear Magnetism. *Oxford Univ. Press, Oxford*, 1961.

[21]. I. Nebenzahl and A. Szoke. Deflection of atomic beams by resonance radiation using stimulated emission. *Appl. Phys. Lett.,* 25:327-329, 1974.

[22]. C.S. Corder. Optical Forces on Metastable Helium. Ph.D. Dissertation. Ph.D. thesis, Stony Brook University, 2014.

[23]. X. Miao. Optical Forces on Atoms with Periodic Adiabatic Rapid Passage Sequences. Ph.D. Dissertation. Ph.D. thesis, Stony Brook University, 2006.

[24]. L.P. Yatsenko, S. Guerin, and H. R. Jauslin. Topology of Adiabatic Passage. *Phys. Rev. A*, 65:043407, 2002.

[25]. J. Elgin. Study of the Velocity Dependence of the Adiabatic Rapid Passage (ARP) Optical Force in Helium. PhD thesis, Stony Brook University, 2015.

[26]. P. Ehrenfest. Bemerkung uber die angenaherte gultigkeit der klassischen mechanik innerhalb der quantum mechanik. 45:455, 1927.

[27]. D. Stack. Optical Forces from Periodic Adiabatic Rapid Passage Sequences on Metastable Helium Atoms. PhD thesis, Stony Brook University, 2012.

[28]. S. S. Hodgman, R. G. Dall, L. J. Byron, K. G. H. Baldwin, S. J. Buckman, and A. Truscott. Metastable helium: A new determination of the longest atomic excited-state lifetime. *Phys. Rev. Lett.,* 103:053002, 2009.

[29]. J. Kawanaka, M. Hagiuda, K. Shimizu, F. Shimizu, and H. Takuma. Generation of an intense low-velocity metastable-neon atomic beam. *Applied Physics B*, 56(1):21-24, 1993.

[30]. B. Winter, S. J. King, M. Brouard, and C. Vallance, A fast microchannel plate-scintillator detector for velocity map imaging and imaging mass spectrometry, *Review of Scientific Instruments* 85, 023306 (2014).

[31]. T. Inaki. Optical phase coherence in the adiabatic rapid passage force. Master's thesis, Stony Brook University, 2017.

[32]. I. Schwartz. Automatic Bias Controller for an Electro-Optic Modulator. MSI thesis, Stony Brook University, 2021.

[33]. Yifan Fang, Edoardo Buonocore , Michael Wahl , and Harold Metcalf. Measurements of velocity-selective resonances from adiabatic rapid passage, *Physical Review A* 107, L051101 (2023) Letter.

[34]. E. Buonocore. Fluorescence Based Doppler Velocimetry. MSI thesis, Stony Brook University, 2022.